Development and Validation of a Systems-Level Cost Optimization Tool for Solar-Powered Drip Irrigation Systems for Smallholder Farms

by

Fiona R. Grant

B.S. Mechanical Engineering
Massachusetts Institute of Technology (2017)

Submitted to the Department of Mechanical Engineering
in partial fulfillment of the requirements for the degree of

Master of Science in Mechanical Engineering

at the

MASSACHUSETTS INSTITUTE OF TECHNOLOGY

September 2019

Signature redacted

Author . . . .
                                        Department of Mechanical Engineering
                                                          August 31, 2019

Signature redacted

Certified by. . . . .
                                        Amos G. Winter, V
                    Associate Professor of Mechanical Engineering
                                        Thesis Supervisor

Signature redacted

Accepted by . . . .
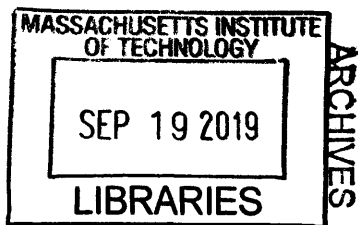   Nicolas Hadjiconstantinou
                            Professor of Mechanical Engineering
                                                Graduate Officer

Development and Validation of a Systems-Level Cost Optimization Tool for Solar-Powered Drip Irrigation Systems for Smallholder Farms

by

Fiona R. Grant

Submitted to the Department of Mechanical Engineering
on August 31, 2019, in partial fulfillment of the
requirements for the degree of
Master of Science in Mechanical Engineering

Abstract

Drip irrigation is a micro-irrigation technology that has been shown to conserve water and significantly increase crop yield. This technology could be particularly beneficial to the world's estimated 500 million smallholder farmers, but these systems tend to be financially inaccessible to this population. Drip systems require costly components including a pipe network, emitters, a pump and a power system; due to limited access to electricity, many smallholder farmers would require off-grid solutions. Designing reliable, low cost, off-grid drip irrigation systems for smallholder farms could significantly reduce the barrier to adoption.

This thesis presents a comprehensive model that holistically simulates the system behavior and cost-optimizes the system design. A custom, low pressure emitter is used in the hydraulic network of these systems. This design tool produces low cost, solar powered drip irrigation systems that are tuned for a specific geographic location and crop type. The model simulates the agronomic, hydraulic, pump and power system behaviors. A PSO algorithm is used along with local economic data to optimize for either the lowest cost design or the design that produces the highest profit from crop yield over the lifetime of the system.

The design must include a properly sized pump and solar panels, and may include energy storage in the form of a battery, a tank or both. The reliability of the design is assessed by simulating its performance over a growing season using local weather and crop data. The extent of the model is explored through sensitivity analysis and a series of sample cases for field sizes ranging from 0.125 to 2 ha. It is shown that the optimization can reduce the life cycle cost of a system by 62% compared to the conventional method for sizing solar powered drip irrigation systems. The potential of the model to inform emitter design and pump selection is also explored. The simulation portion of the model is validated through a set of field trials where two solar powered drip systems were installed and run on small farms in Jordan and Morocco for a full growing season. Future iterations of the model will include

an optimized hydraulic network layout and irrigation operation scheme, as well as more flexible pump selection criteria. Future field work will validate the optimized operation scheme, which will be used along with feedback from the farmers to design a custom controller.

Thesis Supervisor: Amos G. Winter, V
Title: Associate Professor of Mechanical Engineering

Acknowledgments

Acknowledgment of Joint Work

This work was completed jointly with Carolyn Sheline as part of our Master's degree in the GEAR Lab. The theses were prepared in parallel and share much of the same content. I focused on modeling the hydraulic system behavior and pump operation, while Carolyn focused on the agronomic and power system modeling, but we both contributed equally to the simulation analysis and field work.

Contents

List of Figures

9

10

14

List of Tables

Chapter 1

Introduction

1.1 Motivation

Globally, an estimated 500 million smallholder farmers work plots of 2 hectares (ha) or less and produce 80% of the food consumed in Asia and Sub-Saharan Africa [1]. However, only about 10% of global arable land is irrigated [2]. Irrigation can improve yields and decrease water usage for farmers working small plots of land. Traditional methods of irrigation, such as flood and furrow irrigation, involve pouring large quantities of water over the field or into adjacent troughs in the soil. Water can easily evaporate or be absorbed into the soil without reaching the crop roots. If existing agricultural land can be made more productive, the increased output per capita can increase incomes and improve food security.

A drip irrigation system is comprised of a power source connected to a pump that pumps water through a pipe network to the crops. The main pipe connects the pump to the submain pipe, which is connected to lateral pipes that extend along the crop rows. Emitters are attached along the laterals at each crop and release water and nutrients to the root zone of the crop. Pressure compensating (PC) emitters are flow control devices that operate at a relatively constant flow rate above a certain activation pressure. Drip systems with PC emitters can uniformly distribute water to the field, regardless of topology, ensuring that all crops receive the same amount of water. Drip irrigation can reduce water consumption by up to 70% over traditional

methods, and has been shown to increase crop yields by 20-90%, depending on the type of crop [3, 4, 5, 6, 7]. This is especially important in arid regions that are already experiencing water scarcity.

Despite the benefits of drip irrigation, the high capital cost of the systems makes it difficult for smallholder farmers to adopt the technology [8]. The system cost is sensitive to a complex set of co-dependent factors. Many rural farmers have intermittent or no access to grid electricity, which means they would require an off-grid power source, such as solar panels and batteries [9]. Traditional PC emitters have a minimum activation pressure of 0.5-1 bar to operate at their nominal flow rate, which requires significant pumping power, and therefore more expensive pumps and power systems. This thesis considers a drip system with custom, low-pressure emitters that exhibit PC behavior at a minimum pressure of 0.15 bar. This low pressure significantly reduces the pumping power required to operate the drip system [10]. For a given geographic location and crop type, agronomy parameters and local weather patterns determine the water demand of the plant. This informs the hydraulic system design and pump selection, which in turn dictates the power system requirements. Modeling these components as an integrated system can elucidate trade-offs that cannot be exploited if the components are modeled independent of one another.

This thesis presents the development of a drip irrigation system design tool that produces the optimal low cost system for a given location and crop type. The model simulates the system behavior, selects components and then optimizes for the lowest-cost system design. The extent of the model capabilities is explored through sensitivity analysis. This tool is used to design systems for two field trial locations in Jordan and Morocco, and the data from these trials are used to validate and improve the model. The proposed systems-level model is shown to be flexible and robust through simulated case studies. This holistic design method produces drip irrigation system designs that are less expensive than commercial alternatives, and the initial field work both validates the model and suggests avenues for further development.

1.2 Drip Irrigation

Traditional irrigation methods include flood, furrow, and canal irrigation. Flood irrigation involves flooding the entire field with water (Figure 1-1B [11]). Most of the water is absorbed into the ground away from the crop roots or evaporates, making this an inefficient form of irrigation. In furrow irrigation, channels are cut into the ground alongside the crop rows (Figure 1-1D [12]). These channels are filled with water, and although the absorption is more localized, the water can still be lost to evaporation and absorption where the furrows have not yet reached the crop rows. Canal irrigation improves on this slightly with concrete lined channels that carry the water to unlined channels along the crop rows. This reduces the amount of water lost to absorption, but evaporation is still an issue (Figure 1-1A). In all three of these methods, the water is exposed to atmospheric pressure, so the distribution of the water to the crops is highly dependent on the field topology, and some sections of the field may routinely receive more water than others.

A sprinkler system is a pressurized method of irrigation that delivers water through a pipe network to sprinklers in the field, which spray water over the crops (Figure 1-1F [13]). Due to the pipe network, no water is lost to absorption as it travels to the field, but the water can still evaporate from the sprinklers and wind can blow the water droplets away from the crops. This is a more efficient form of irrigation, but typically more expensive due to the pipe network and sprinklers. In any of these irrigation methods the water may be pumped or gravity-fed. Gravity-fed irrigation involves water stored at a height, which could be in the form of an elevated water tank or an entire dam, depending on the size of the field (Figure 1-1E).

Drip irrigation is similar to sprinklers in that it requires a pipe network, but instead of spraying the water over the crops, drip emitters placed along the pipes at each crop release a controlled volume of water directly to the root zone of the crop (Figure 1-1C). This significantly reduces the amount of water lost to evaporation and absorption away from the crop. Fertilizer is typically introduced into the water source and distributed through the irrigation system in a process called fertigation.

23
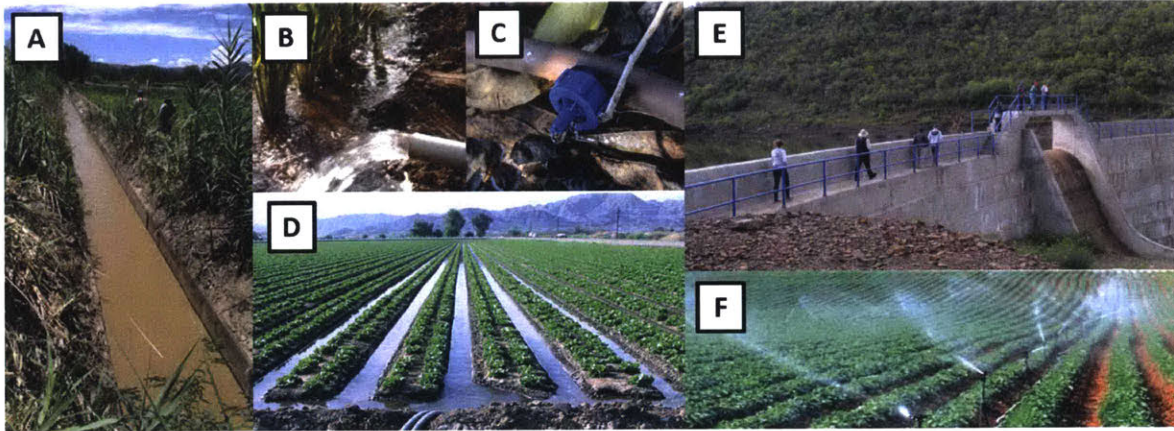
Figure 1-1: Examples of various irrigation methods. More traditional methods such as canal (A), flood (B) and furrow (D) irrigation lose water to evaporation and absorption. Methods with a pressurized pipe network include sprinklers (F), which can still lose water to evaporation, and drip (C), which minimizes water loss. Any of these methods can be gravity-fed (E) with an elevated tank or dam.

This means drip irrigation systems can deliver an exact amount of nutrients directly to the crops, without runoff or uneven distribution.

Although drip irrigation is a more efficient and controlled irrigation method, it only makes up 6% of the global irrigated area [14]. Drip is not widely adopted among smallholder farmers because of the high initial investment and additional maintenance costs [15, 16]. Typically the pressure required for a drip system with existing emitter designs is too high to be gravity-fed. Many smallholder farmers have intermittent or no access to electricity, so the power system must be off-grid for reliable irrigation [9]. Drip systems also require additional maintenance compared to other irrigation methods. Emitters have small internal flow paths, so the water typically needs to be filtered and emitters need to be routinely checked for clogging. All this amounts to an irrigation system that has a high capital cost and additional maintenance and labor costs. Reducing the cost of these systems and ensuring they can operate reliably off-grid would make drip irrigation more accessible to smallholder farmers.

1.3 Stakeholders

The target users of these systems are smallholder farmers who may lack access to the capital and technical knowledge to purchase and maintain drip irrigation systems. Smallholder farmers work less than 2 ha of land, growing crops for either subsistence or profit. In Jordan and Morocco, the two countries considered in this study, there are programs to encourage adoption of more efficient irrigation methods by educating farmers about these technologies and offering subsidies. However, farmers often lack the capital to purchase such systems and have difficulty obtaining loans from banks. Depending on the specifications of the program, this can make it difficult for farmers to take advantage of the subsidies [15, 16].

The key stakeholders in this process are the company that produces the drip systems, an organizational body that coordinates distribution and subsidies for farmers, and the farmers themselves. The main priorities of each stakeholder have been identified through conversations with two agricultural research organizations: Methods for Irrigation and Agriculture (MIRRA) in Jordan and the International Center for Agricultural Research in the Dry Areas (ICARDA) in Morocco. Jain Irrigation Ltd., the second largest irrigation company in the world, and local smallholder farmers in Jordan and Morocco were also consulted. An example stakeholder map that shows how these groups might interact is given in Figure 1-2.

The priority of the company is to make a profit and continually improve the system design. The priorities of the government agency or NGO are to expand access to more efficient forms of irrigation and conserve water resources. The priority of the users is to increase yield and income, decrease their use of water, fertilizer and other resources, and avoid a high capital investment or added maintenance costs. An irrigation company would design, source, and assemble drip kits for farmers in a specific location. A government agency or NGO would handle distribution of these kits to the farmers and coordinate subsidies for the farmers to encourage adoption. This agency would also collect user feedback and system performance data for the company. A training program must be established to install the systems and provide

25
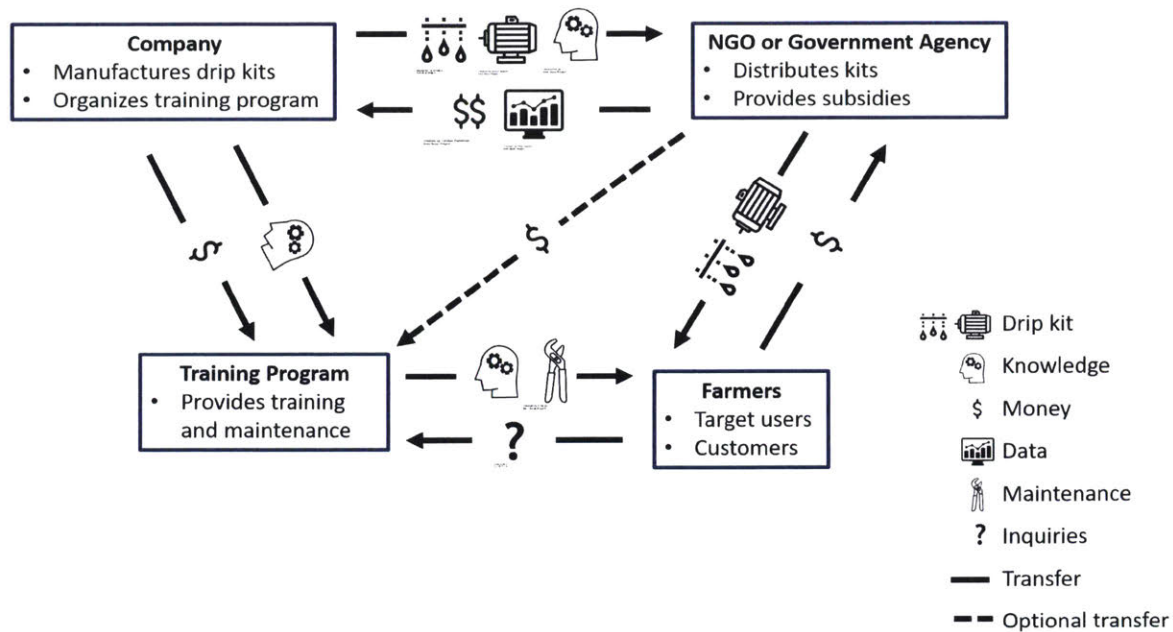
Figure 1-2: An example stakeholder map for the development and distribution of solar powered drip irrigation systems.

farmers with initial training and continued technical support. This program would be organized and funded by the company, potentially with additional funding from the government agency or NGO. This proposed set of stakeholder interactions would ensure that smallholder farmers have access to low-cost drip irrigation technology as well as the knowledge to maintain and profit from it throughout the system lifetime.

1.4 Previous Work

Shamshery (2018) presents a low-pressure, online PC drip emitter design with an activation pressure one seventh that of existing commercial products [17]. These emitters have been manufactured and tested in the field, as shown in [18], and are used exclusively in the systems-level model presented in this thesis. Their low activation pressure significantly reduces the operating pressure required to operate the drip system, allowing for smaller pumps and power system capacities in the design. Ultimately, the use of low-pressure emitters in the model allows for lower cost solar powered drip irrigation systems to be designed.

Bakelli (2011), Muhsen (2018), Kelley (2010), Deveci (2015), and López-Luque (2015) all consider the design and optimization of solar powered pumping systems but impose limitations on their models [19, 20, 21, 22, 23]. Bakelli (2011) defines a demand-based reliability constraint and an economics model for calculating the system life cycle cost (LCC), which are useful for framing the optimization problem. The hydraulic behavior of the system is estimated using a polynomial fit to data, rather than fluid mechanics, and the optimization method is a simple minimum point search. This limits the scope of cases the model could design for and the system design space. Muhsen (2017) proposes a multiobjective optimization scheme that minimizes LCC, a reliability metric called the loss of load probability (LLP), and excess water volume. While the optimization algorithm is more advanced, the three minimization criteria are weighted subjectively. The paper also defines the system components a priori, rather than selecting the components within the optimization scheme, and only optimizes for the number of panels and tank capacity. Kelley (2010) assesses the feasibility of solar powered irrigation, assuming a system with a well source, and using average irradiance and maximum crop water requirement for five cases studies. The system designs are not optimized, but local economic data are used to link designs to their locations. This is a concise, first-order assessment that is a useful benchmark for a more detailed sensitivity analysis. Deveci (2015) discusses the design of a low-cost, solar powered drip irrigation system for small farms using a systems-level approach. The study assumes a system that includes batteries and a tank, assumes the irrigation time required and only considers component capital cost. The systems-level approach is useful for framing the problem, but the system description is over-simplified by its assumptions. López-Luque (2015) discusses the optimal design for a solar-powered irrigation system using an olive orchard case study. The paper uses various sub-models to simulate the system while implementing a deficit irrigation scheme and optimizing for profitability. This study shows that with deficit irrigation the cost of the solar-powered pump is able to be reduced, but the model is limited with a very specific system design that does not include energy storage options and only considers non-pressure compensating emitters.

Other studies focus on specific aspects of this design problem. Almeida (2018) produces a pump selection method for solar powered irrigation systems, with the goal of pumping as much water as possible [24]. The method suggests pairing a variable frequency drive (VFD) with a pump to ensure a wide potential operating range. The method becomes useful in the context of this study when selecting pumps that must pump to the PC drip network as well as to a water storage tank. Villalva (2009) presents a comprehensive and instructional approach to accurately model photovoltaic (PV) array operation under various temperature and irradiance conditions [25]. Several studies have explored how to model the life cycle cost of these systems. Lai (2017) and Muhsen (2017) both propose detailed cost models that consider initial investment, maintenance, replacement, interest, and inflation over the lifetime of the system. The cost equations used in this study are based off of these definitions [26, 20].

This study builds upon previous work on solar powered drip irrigation systems by adding resolution and flexibility to the model. Local hourly weather data are used to simulate the PV array behavior and calculate a daily water demand based on crop properties and growth. The behavior of the hydraulic network is simulated using fluid mechanics equations to allow for any pipe network configuration. The custom ultra-low pressure PC emitters used in the model shift the system operating point into a lower pressure regime than a system with conventional PC emitters. The pump selection and power system design are optimized in a particle swarm optimization (PSO). Local economic data are used in a life cycle cost objective function and a limit on the LLP constrains the optimization. By using high resolution datasets and simulating the behavior of the individual system components, this holistic model offers a broader design space to explore and optimizes for a solution that is intrinsically linked to a given location and crop type.

Chapter 2

System Components

2.1 Drip System Overview

A drip irrigation system consists of a water source, a pump, a power system, a hydraulic pipe network, filters, a fertigation unit, and emitters (Figure 2-1). The hydraulic components are connected by a network of pipes that have progressively smaller diameters. The main typically has the largest diameter to reduce pressure losses along its length as water flows to the field. A sand and disk filter are typically placed after the pump to reduce emitter clogging. This is followed by a fertigation unit that periodically injects fertlizer into the network. The type, amount and frequency of fertilizer depends on the crop. At the field, the submain pipe lies along one dimension of the irrigated plot. The submain can be the same or slightly smaller in diameter than the main. The laterals, which have the smallest diameter, branch off of the submain and run down the rows of crops, with one or more emitters at each crop. The spacing of the lateral rows, the spacing of the emitters along the lateral, and the number of emitters per crop are agronomic parameters that depend on the type of crop and the soil properties. The emitters exhibit PC behavior, which means that above a certain activation pressure, the emitter flow rate is constant. This effectively means the entire drip system will operate at a fixed flow rate. The emitters considered in this work have been designed to operate at 0.15 bar, one-seventh the activation pressure of conventional online PC emitters [17].
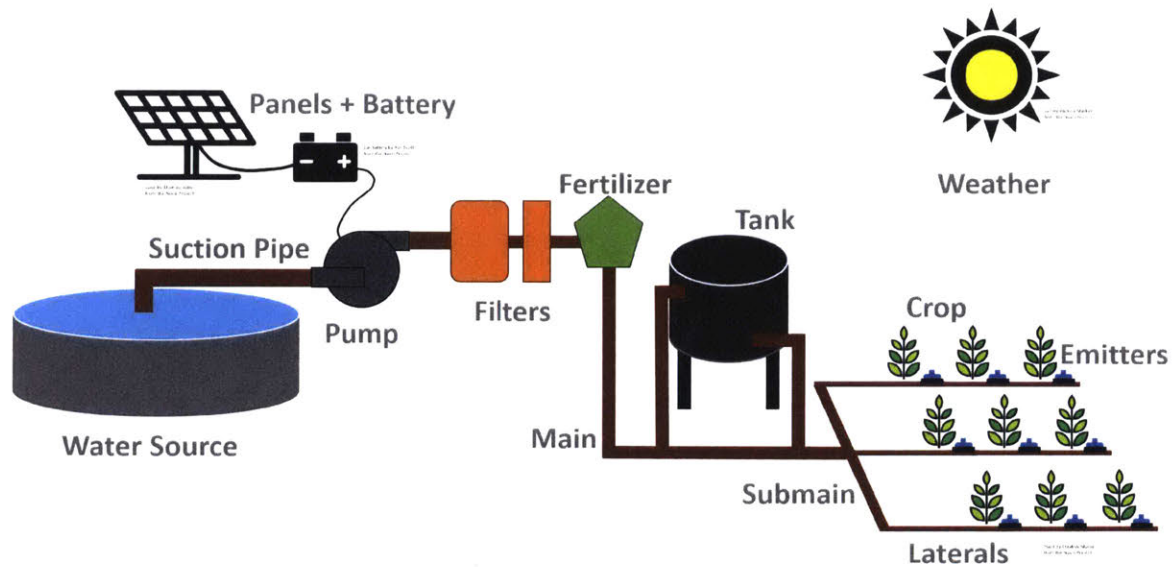
Figure 2-1: A diagram of a solar powered drip irrigation system shows the relevant components and subsystems.

Single-speed AC pumps are ubiquitous and about 62% of the global irrigated area draws from surface water sources [2]. The pressure drop in the hydraulic network will fluctuate over time as the water filters become dirty, the fertigation unit is used and the emitters clog. Therefore, the pump must be paired with a VFD to ensure its operating range can accommodate all the states of the system. The pump also requires a controller that can regulate the pump operation and program the irrigation schedule. The power system consists of a solar panel array and, in some cases, energy storage in the form of a battery, a water tank, or both. It is beneficial to have a Maximum Power Point Tracker (MPPT) attached to the panel array to boost efficiency by ensuring that the panels always output the maximum possible power for the given weather conditions. The selection and capacity of these components is highly dependent on the geographical location and the way the components interact as the system operates, which is discussed in Section 2.2.

2.2 Subsystems

The irrigation system components can be be grouped into four interdependent subsystems that interact in a loop: an agronomy subsystem, a hydraulic subsystem, the pump, and the power system. The crop type, growth cycle, and water and nutrient needs, as well as the local weather patterns and soil properties are all agronomic considerations. The local solar irradiance, temperature, wind speed, and humidity will determine the evapotranspiration rate of the crops, and rainfall will offset the amount of water the crop needs from the drip system. The type of crop and soil properties will determine the spacing requirements of the drip network, which will in turn dictate the hydraulic behavior of the system. The crop water demand, emitter properties, and network layout will determine the hydraulic operating point, and the selected pump must be able to operate reliably at this point. The characteristics of this pump will determine the power requirement at different head conditions the pump encounters due to the the filters, fertigation, and emitter clogging. This power requirement will dictate the capacity of the power system components, namely the solar panels, batteries, and tank. Given this is a solar powered system, the irradiance and weather patterns will determine the power available to the system, thus completing the subsystem loop (Figure 2-2).

This is a dynamic, interdependent system that makes for an interesting optimization problem. The objective is to reduce the total life cycle cost of the system. Although the relationships between the subsystems make modeling more complex, these relationships also introduce design flexibility and expand the solution space. The model can simulate the hydraulic behavior of any hydraulic layout which allows for a variety of crops, hydraulic components, and field shapes and sizes. Calculating the crop water demand using local weather data links the hydraulic load on the system to the available solar power and ensures the design is customized for a specific location. Battery and tank storage allow for irrigation at times of low irradiance or at night. Due to the PC behavior of the emitters, the flow rate of the drip system is fixed, but the pump could fill a tank quickly at higher flow rates, making use of excess
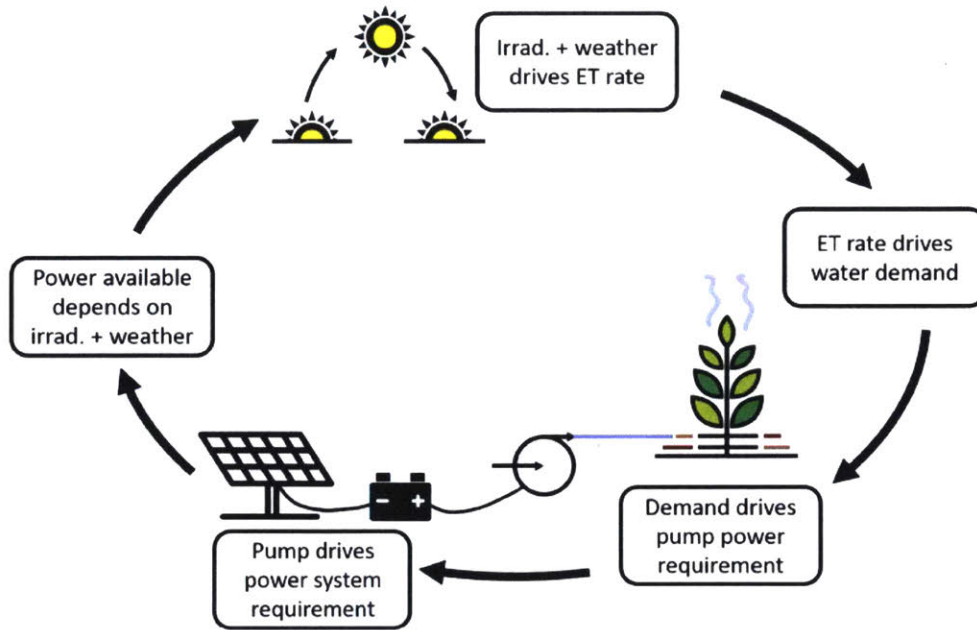
Figure 2-2: The cyclic relationship of the four interdependent subsystems. The agronomic requirements of the crop are influenced by local weather patterns, and dictate the hydraulic load on the pump. This in turn dictates the capacity requirements for the power system, which is also dependent on the weather throughout the irrigation season.

solar irradiance, or slowly at lower flow rates, making use of times of low irradiance when there is not enough power to pump directly to the drip system. The field size, crop water demand, and local weather will together determine the capacities of the power system components. By exploiting the subsystem relationships in simulation, the drip system can be cost-optimized for any given location, crop type, and field layout.

Chapter 3

Methods

3.1 Model Formulation

The systems-level model optimizes a drip system design for a specific "case," and is divided into modules that represent the subsystems discussed in Section 3. Each module has a set of inputs, which can include datasets and outputs from other modules, and a set of outputs which is passed to other modules as inputs or for evaluation. The modules and their inputs and outputs are discussed in detail in the following sections. A case is defined by the location, soil texture characteristics, length and diameter of the main, submains and laterals, crop spacing, emitter properties, the pressure drop across the filters and fertigation unit, and the start date of irrigation.

The architecture of the model can be broadly divided into three phases: simulation, design and performance (Figure 3-1). In simulation, the agronomic and hydraulic behavior of the case is established. Information about the local weather and crop properties, such as growth stages and water requirements, are passed into the agronomy module, which calculates the parameters necessary for the daily crop water demand. In parallel, the dimensions of the hydraulic network and the emitter flow properties are passed into the hydraulic module, which simulates the hydraulic behavior of the network and produces a hydraulic system curve. This module is not limited to PC emitters - it can also simulate non-pressure compensating (NPC) emitters, sprinklers, or any other irrigation device that works in a pipe network. Both

the daily crop water demand and the hydraulic system behavior become inputs for the modules in the design phase. In this phase, a suitable pump is selected based on the pipe network hydraulic requirements. The pump specifications and the local weather data are passed into the power module which sizes a solar panel array, a tank, and a battery. The solar panels are required, but the tank and battery can be omitted to produce a direct drive power system. The power system module also runs a simulation of how this drip system would operate over the course of one growing season. Up to this point, no optimization has occurred. This combination of pump and power system components is just one possible design that must be evaluated in the performance phase. The life cycle cost of the entire drip system and the reliability with which it meets the crop water demand are calculated and passed into the crop yield module. This module calculates the yield based on the amount of water delivered to the crops over the simulated season and the predicted revenue over the lifetime of the drip system, assuming that season is representative of how the system will perform every year.

A custom particle swarm optimization (PSO) algorithm is used in MATLAB to generate possible designs and determine the trajectory of the design vector. The details of the optimization are discussed further in Section 3.3. The PSO was modified from an algorithm that was successfully used to cost-optimize solar powered village-scale desalination systems [27, 28]. The PSO operates between the design and performance phase, iteratively offering designs and evaluating their performance until it converges on a solution (Figure 3-1). The objective of the optimization can either be set to minimize life cycle cost or to maximize the profit over the lifetime of the system. With the former, the crop yield module is not used in the optimization. Crop yield is dependent on many variables, which makes it difficult to model accurately, and data on local crop prices may not always be available. It is useful to estimate the profit a farmer could make with one of these systems, but being able to remove the yield module removes a layer of uncertainty and complexity in the design process.

The PSO only optimizes the pump and power system configuration, and notably does not optimize the hydraulic network or the drip system operation scheme. The

34
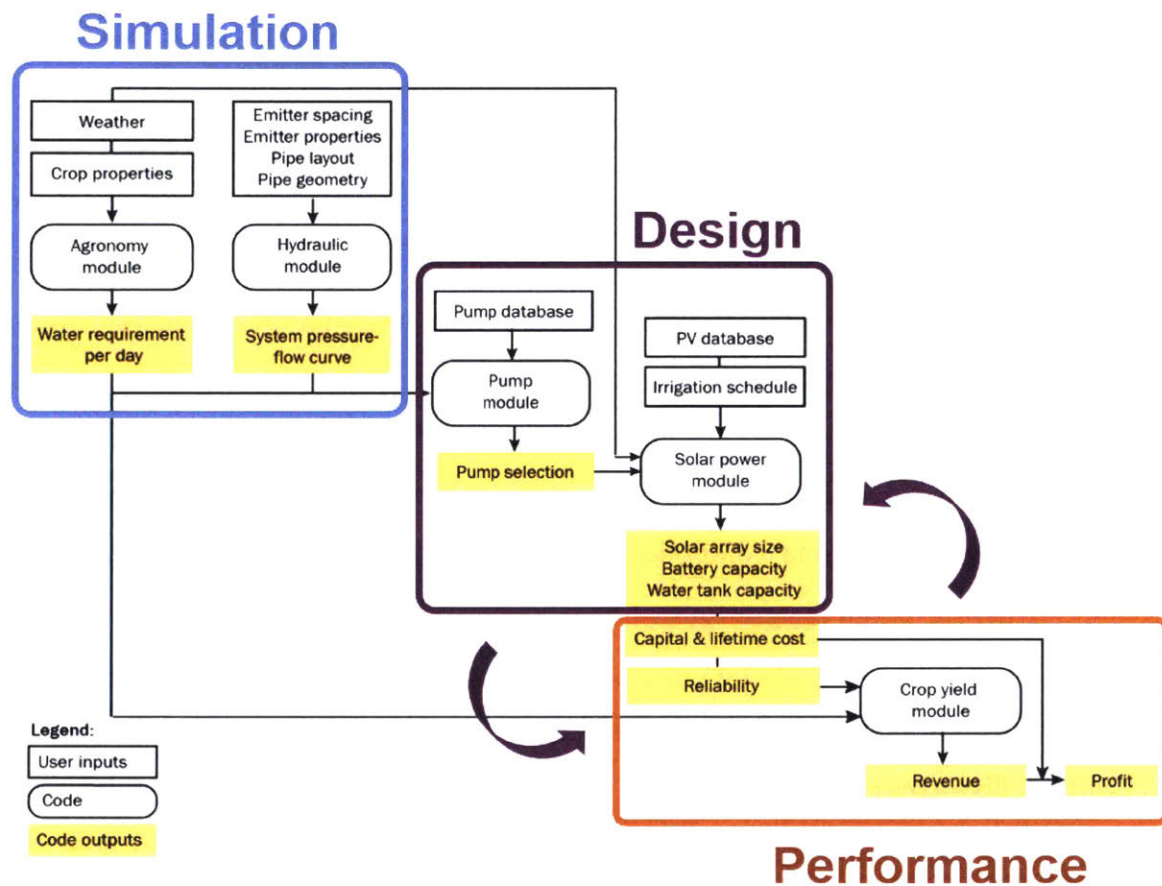
Figure 3-1: The system model architecture and its three phases: simulation, design and performance. The modules in the first two phases represent the four subsystems, and the last phases assesses the performance of the proposed system design. A PSO algorithm iteratively proposes designs until the solution converges on the design with the best performance. The performance can either be defined as the life cycle cost, or the profit from crop yield. Note that the crop yield module is only used for the profit-based optimization.

hydraulic network, once simulated, is considered fixed. The purpose of this is twofold. First, the layout of the hydraulic network is typically left to the discretion of the farmer whose agronomic knowledge and familiarity with the field will inform these decisions. Furthermore, some farmers will already have pipe networks that they use with electric or diesel pumps. Second, the optimum of the hydraulic network is known. For a given field size and crop type, the layout that minimizes pipe materials for the lowest operating pressure will be the most cost effective. In future generations of the model, the hydraulic network can be optimized independent of the rest of the system and the result can still be used as an input to the design phase shown here. Similarly, the simulated operation of the drip system for a season in the power module is predetermined. This means that the operation sequence for powering the pump, filling the tank and charging the battery is fixed. This operation scheme has binary checks based on available solar power and the daily water requirement, but it is not optimized. Eventually the algorithm should be able to make decisions about when and how to operate different components such that the system operation parameters become variables within the optimization.

The first step to using the model is defining a case. For continuity, a sample case has been selected as an example for the remainder of this chapter. The case is a 1 ha field of olive trees in Morocco. The trees have a 5 m by 5 m spacing and there are two low-pressure, PC emitters at each crop. The emitters have a rated flow rate of 8 Lph and an activation pressure of 0.15 bar. The module outputs shown are the results for this case, but would be similar in form for any case.

3.2 Subsystem Modules

3.2.1 Agronomy

The agronomy module calculates the crop evapotranspiration, which is necessary to determine the crop water requirement. This module is particularly detailed and flexible, as it calculates the parameters on a daily basis and allows for a different location,
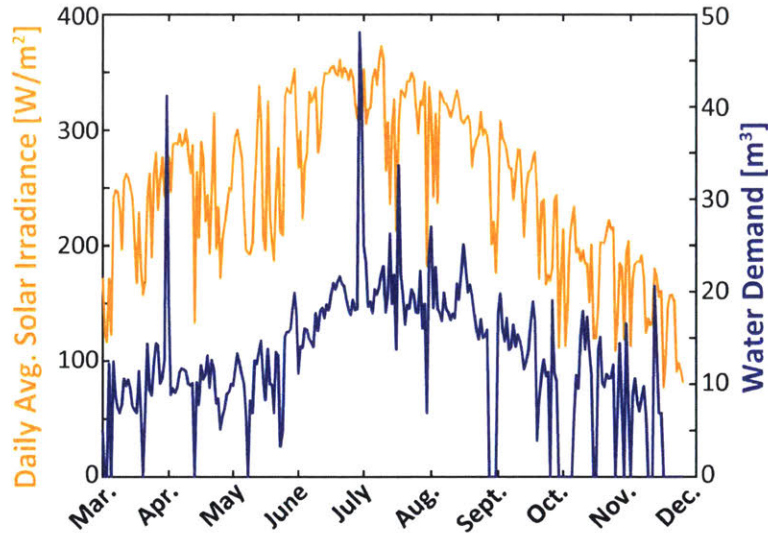
Figure 3-2: Field data shows how the daily water demand varies over the season, tracking the available solar irradiance. This illustrates the link between local weather patterns, crop water demand, and the resulting hydraulic load on the system.

crop, soil texture, sow date, and irrigation type to be specified. It is important to calculate the water demand on a daily basis, rather than use an average or maximum demand, because it varies with the daily weather parameters such as solar irradiance (Figure 3-2). The water demand calculation does not exactly follow the irradiance, as it is also determined by other weather and crop parameters. The large spikes in the water demand in April and July are due to changes in the water uptake in the root zone of the crop. By using a more detailed calculation, the system design can be more closely tuned to the crop needs. The water demand calculation is discussed further in Section 3.2.6.

In the current model implementation, crop data from [29] and typical meteorological year weather files (ASHRAE IWEC2) from [30] are used. These weather files give representative hourly average weather values based on weather data collected for that location over at least the past 12 years and up to the past 25 years. The important weather parameters used in this model are air temperature (T), relative humidity (RH), solar radiation (G_{solar}), wind speed (u), and precipitation (P). The crop tables, which were created based on similar tables in [29] and [8], include the crop growth stages, root depth, plant height, depletion fraction, and crop coefficients.

In order to calculate the crop water requirement, it is necessary to compute a water balance on the soil (Section 3.2.6). Part of the water balance is the crop evapotranspiration (ET_c), which is calculated from the crop coefficient (K_c) and the reference evapotranspiration (ET_0), shown in Equation 3.1.

$$ET_c = K_c \cdot ET_0 \tag{3.1}$$

ET_0 is the evapotranspiration [mm/day] for a grass reference crop of 0.12 m height. It is calculated using the meteorological data and the Penman-Monteith equation [29]:

$$ET_0 = \frac{0.408\delta(R_{net} - G) + \gamma C/(T + 273)u_2(e_s - e_a)}{\delta + \gamma(1 + 0.34u_2)}. \tag{3.2}$$

R_{net} is the net radiation at the crop surface [MJ/m^{2}day], G is the soil heat flux density [MJ/m^{2}day], T is the daily or hourly average air temperature at 2 m height [ ], u_2 is the wind speed at 2 m height [m/s], e_s is the saturation vapor pressure [kPa] at air temperature T, e_a is the actual vapor pressure [kPa], δ is the slope of vapor pressure curve [kPa/] at air temperature T, $\gamma = 0.665 \times 10^{-3}$ is the psychrometric constant [kPa/], and P is the atmospheric pressure [kPa]. Details of the calculations of specific terms in the Penman-Monteith equation can be found in [29], Chapter 3. Meteorological variables are extracted directly from weather data whenever possible. At minimum, temperature, relative humidity, wind speed, and total solar shortwave radiation must be provided in the weather file.

Hourly weather data are adapted to the daily evapotranspiration calculation (Eq. 3.1) as follows. Vapor pressure and the slope of the vapor pressure curve are computed using minimum and maximum hourly temperatures and relative humidity levels recorded throughout the day. Net radiation at the crop surface (R_{net}) is computed as described in [29], with the incoming shortwave radiation taken directly from the weather data file. Shortwave radiation is summed over 24 hours, and wind speed is averaged. The case studies in this thesis use daily ET_0 only. K_c, the crop coefficient, is used to scale ET_0 to ET_c (Eq. 3.1). K_c is a function of the crop and the stage of its development. The length of the development stages and K_c values corresponding

to each stage ($K_{c,ini}$, $K_{c,mid}$, $K_{c,end}$) are pulled from the crop tables. Initial and mid-season stages have constant coefficients, with a linear change in coefficient during the crop development stage between $K_{c,ini}$ and $K_{c,mid}$ and late season between $K_{c,mid}$ and $K_{c,end}$. When climate conditions are different from the climates used for tabulated K_c values such that $RH_{min,mean} \neq 45\%$ or $u_{2,mean} \neq 2.0 m/s$, $K_{c,mid}$ and $K_{c,end}$ are adjusted (Eq. 3.3), provided that the tabulated value of $K_{c,end(Tab)} \geq 0.45$:

$$K_{c,mid/end} = K_{c,mid/end(Tab)} + (0.04(u_{2,mean} - 2) - 0.004(RH_{min,mean} - 45))(\frac{h}{3})^{0.3}, \quad (3.3)$$

where $K_{c,mid/end(Tab)}$ is the tabulated value for $K_{c,mid}$ or $K_{c,end}$, h is the mean plant height during the mid/late-season stage [m] (tabulated), and values of $u_{2,mean}$ and $RH_{min,mean}$ are calculated for the corresponding growth stage. Custom crop coefficients and development stage lengths can also be entered directly into the crop tables if more accurate local data is available.

After the daily ET_c is calculated for the given crop [mm/day], it is converted to the volume of water that needs to be delivered to the field [m^3/day]. Equation 3.4 describes how to convert irrigation (I) in [mm/day] to a volumetric daily water requirement (V_{irri}).

$$V_{irri} = f_w \cdot A_{field} \cdot I/1000, \quad (3.4)$$

where f_w is the soil wetted fraction, which is assumed to be 0.3 for drip irrigation and A_{field} is the field area that is being irrigated [29]. This calculated daily water demand is the key parameter that links the subsequent drip system design to a location and crop type.

3.2.2 Hydraulics

The hydraulics module takes in details about the pipe lengths and inner diameters, as well as the pipe network geometry (Figure 3-1). The pipe layout is set by the

length of the suction pipe, the length of the main between the pump and the field, and a set of subunits whose area is defined by the length of the submain and the length of the laterals. The spacing of the laterals, the spacing of the emitters along each lateral, and the number of emitters per crop are specified based on agronomic recommendations for the crop. The example case includes two subunits of 0.375 ha and a third of 0.25 ha, with a 5 m by 5 m crop and row spacing and two emitters per olive tree (Figure 3-3). This emitter layout is based on suggestions from local agronomists during the field trials. The pipe lengths and number of subunits are somewhat subjective decisions. In all the simulated cases, the laterals were set to 50 m and the length of the submains were made as long as possible to meet the total area requirement. Increasing the length of the submain will incur less of a pressure loss than increasing the length of the laterals because pressure loss in a pipe scales inversely with the pipe diameter squared, and the laterals have the smallest diameter. Not shown in this schematic are additional hydraulic components that incur pressure losses in the system, namely the disk and sand filters, the fertigation unit, elbows, tees, connectors, and valves. Each hydraulic network will contain different quantities of these additional components, so the total additional pressure losses are estimated as part of the case definition that is passed into the hydraulic module.

The final inputs to the hydraulics module are the emitter properties. PC emitters are flow control devices that operate at a constant flow rate above their activation pressure. A drip network of PC emitters will have a constant flow rate once the emitter at the end of the last lateral, which is the furthest from the pump, has reached this activation pressure. The nominal flow rate, activation pressure, flow coefficient, k, and pressure compensation exponent, x, of the custom low-pressure, PC emitters are inputs to the hydraulic module [17]. The module simulates the hydraulic behavior of the defined drip network through an iterative calculation that determines the flow and pressure at all points in the pipe network. The major losses in the pipe network are calculated with the Darcy-Weisbach equation (Eq. 3.5) and the minor losses at the start of the submain are estimated using $K = 1$ for tee fitting losses (Eq. 3.6) [31].

40
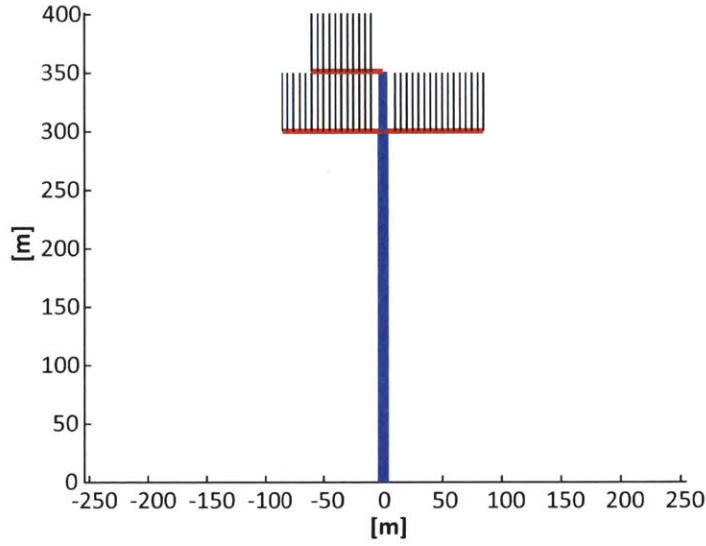
Figure 3-3: An example hydraulic network layout for the 1 ha sample field shows the main pipe (blue), submain pipes (red) and laterals (black). The emitters (not shown) are spaced along the laterals. The pipe diameter decreases for each type of pipe. The network geometry is subjective, but in this study, the laterals are 50 m and the submain lengths are selected to meet the area requirement.

$$\Delta P_{major} = f_d \frac{L}{D} \frac{\rho V^2}{2} \tag{3.5}$$

$$\Delta P_{major} = K \frac{\rho V^2}{2} \tag{3.6}$$

The Darcy friction factor, f_d, for turbulent flow in pipes is calculated using the Swamee-Jain formula (Eq. 3.7), where Re is the Reynolds number, D is the pipe inner diameter and ϵ is the pipe roughness [32].

$$f_d = \begin{cases} \frac{64}{Re} & for \ Re < 2300 \\ 0.2 \times \left[\log_{10} \left(\frac{\epsilon}{3.7D} + \frac{5.74}{Re^{0.9}} \right) \right]^{-2} & for \ Re > 2300 \end{cases} \tag{3.7}$$

The emitter flow behavior is modeled as linear when $0 < P < P_{act}$ and as following the curve $Q = kP^x$ when $P \geq P_{act}$. Here, k is the flow coefficient, x is the pressure compensation exponent, and P_{act} is the activation pressure. A constant 0.01 bar is added for the pressure loss due to additional pipe fittings and 0.3 bar is added for the
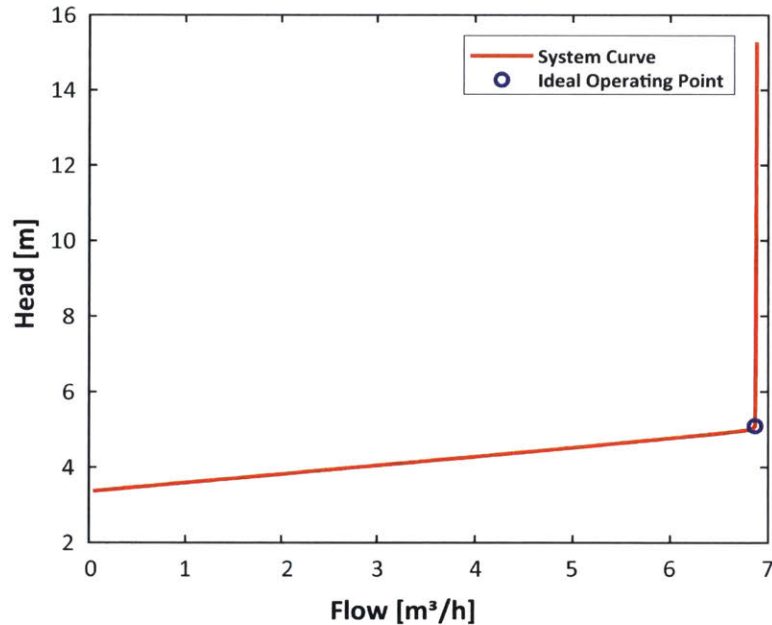
Figure 3-4: The hydraulic system curve for the 1 ha sample case shows the pressure compensating behavior introduced by the low pressure PC emitters. The flow rate increases with pressure until the last emitter has reached its activation pressure, at which point the flow remains constant. The ideal, minimum power operating point for the system is just after this slope change (blue circle).

pressure drop across the filters and fertigation unit. Pressure losses due to flow over the emitters are neglected, and the simulation only models steady state behavior. The hydraulic calculation is run for a range of input pressures until the flow rate solution converges to within 1 L/h of the flow at the entrance of the submain. This iterative flow calculation is discussed in further detail in [31].

The module outputs the system hydraulic curve, as shown in Figure 3-4. The flow rate is the drip network flow rate and the pressure head is the input pressure to the system from the pump. The flow rate increases gradually until the last emitter, the emitter at the end of the furthest lateral, has reached the activation pressure. As the input pressure increases beyond this point, the flow rate remains constant, which means the required hydraulic power must be increasing. Therefore, the ideal system operating point is the minimum power point where the last emitter has just reached activation and the flow rate becomes constant (Figure 3-4). This operating point becomes the input to the pump module and is used to select a pump for the system.

3.2.3 Pump & Power System Overview

The pump module is the beginning of the design phase, which selects and sizes the pump, solar panel array, battery, and tank. The algorithm must select a pump and some non-zero panel area, but it has the option to select zero capacity for the battery and tank. In addition to capacity, each of these components has parameters that define its performance. Panel performance is defined by its efficiency, which changes with the weather conditions. The weather-dependent panel efficiency is simulated with a single-diode model as described in Section 3.2.5. A single controller efficiency is also applied to the power from the panel array to represent the electrical efficiency within the MPPT, charge controller and pump controller. The battery is defined by its state of charge (SOC), or the energy it stores at any given time, and the conversion efficiency when its charging and discharging. Both of these parameters are also influenced by temperature, but that dependence is not modeled here. The pump is defined by its hydraulic performance curves and the efficiency with which it converts electrical power into hydraulic power at the operating flow rate and pressure. The tank is defined, similar to the battery, by its state of fill (SOF), which is the volume of water it stores at any given time. When this water is released to the system, it will have a pressure based on the height of the water stored and a flow rate that is fixed by the PC behavior of the hydraulic network described in Section 3.2.2.

The energetic exchange between these components is shown in Figure 3-5. The panels generate power from the available solar irradiance, which is electrically regulated by a series of controllers. This can go to the pump or, if the system has a battery, the excess power can be stored as energy in the battery. The battery can be discharged to power the pump, which can pump water directly to the hydraulic network or, if there is a tank, store it to be released to the system later. As previously mentioned, the order in which these events occur is predetermined and described in further detail in Section 3.2.5.
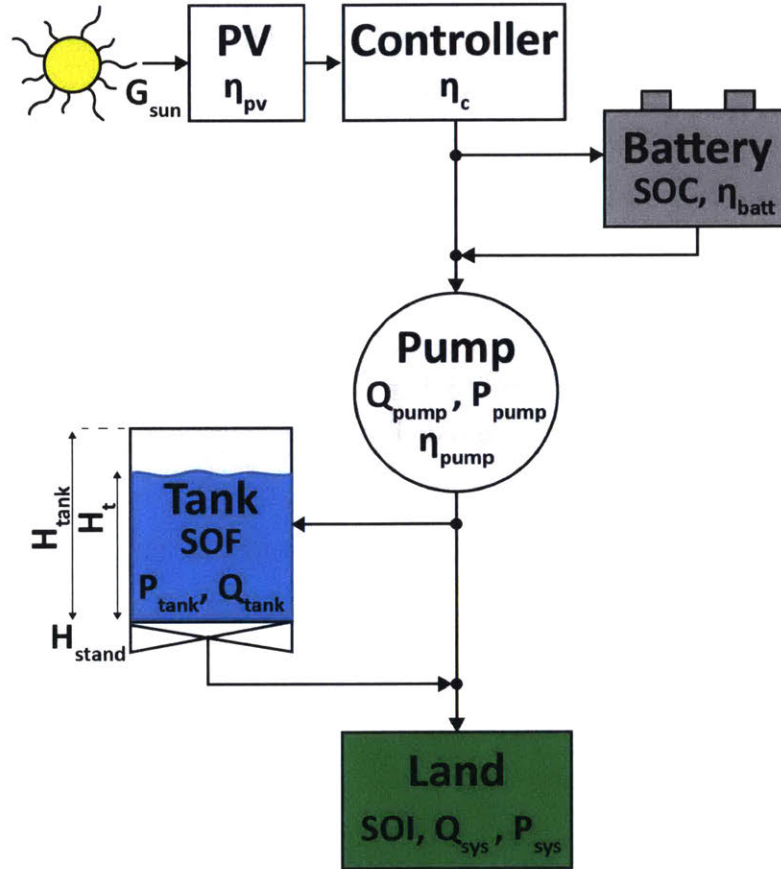
Figure 3-5: A diagram of the design components and their parameters shows how the components relate to one another energetically. The panels are defined by their efficiency, η_{PV}, the controller is represented by η_c, and the battery has a state of charge vector (SOC) and an efficiency, η_{batt}. The pump is characterized by its operating point at Q_{pump}, P_{pump}, and its efficiency, η_{pump}. Water is pumped to the tank at the operating point Q_{tank}, P_{tank}. The tank has a height, H_{tank}, and its operating pressure depends on the stand height, H_{stand}, the height of the water, H_t, and its state of fill vector (SOF). The battery and tank are both optional energy storage options that may be added to the power system design. The drip network operates at Q_{sys}, P_{sys}, and there is a state of irrigation vector (SOI) that describes the volume water delivered to the field at any given time.

3.2.4 Pump Selection & Operation

The pump module takes in the system operating pressure and flow rate from the hydraulics simulation and selects a pump from a database of pump options. The database contains the pump performance curves and specifications, which include the maximum power and flow rate, the motor speed, and the best efficiency (BEP) point. The pumps in the database are sourced from Xylem Inc. due to their readily available datasheets, but any pump can easily be incorporated into the database. Currently, the database is made up of exclusively surface, centrifugal pumps with AC motors. This is because the field trials in this study use surface water sources and single speed AC pumps are ubiquitous, which means they are easier to purchase and repair locally than DC pumps. In the future, the database will be expanded to include pumps that are submersible, positive displacement, and have DC motors.

Typically, a pump is sized for a system by finding the point where the pump performance curve intersects with the system hydraulic curve. If this intersection point has a flow rate between 85-110% of the BEP flow rate of the pump, it is within the preferred operating range (POR) of the pump. This means the pump will operate to its rated lifetime and efficiency without degradation due to cavitation [33]. Here, this range is expanded to 65-110% of the BEP flow rate to provide a wider range of pump options for each simulation case. For a given case, all of the feasible pumps with performance curves that intersect the hydraulic system curve within this range are found and become options in the design. To simplify this process and speed up the optimization, the database contains "representative pumps" of various sizes such that seven test cases, ranging in field sizes from 0.125 to 2 ha, each have one or more feasible pumps. All of the pumps are assumed to have a lifetime of 5 years. In reality, operating outside the POR decreases the lifetime of the pump, but this effect is not yet modeled in detail.

The system flow rate will remain constant, but as discussed in Section 3.2.2, the operating pressure of the pump will fluctuate as the filters get dirty and the fertigation unit is used. Therefore, it is assumed that these pumps are paired with

a VFD in order to shift the performance curve to meet the system operating point. Changing the motor frequency changes its rotational speed and the operating speed of the pump. This is modeled using the affinity laws for centrifugal pumps, shown in Equations 3.8-3.10 [34]:

$$\frac{Q}{Q_{ref}} = \frac{N}{N_{ref}} \tag{3.8}$$

$$\frac{H}{H_{ref}} = \left(\frac{N}{N_{ref}}\right)^2 \tag{3.9}$$

$$\frac{P}{P_{ref}} = \left(\frac{N}{N_{ref}}\right)^3 \tag{3.10}$$

The flow rate, Q, scales proportionally with the speed ratio, where the reference speed, N_{ref}, is the known pump speed and N is the speed of the new operating curve. The pressure head, H, scales with the square of the speed ratio, and the power, P, scales with the cube of the speed ratio. The key assumption these laws make is that the pump is running at approximately the same efficiency at the operating point on the new curve as on the reference curve. In the model, the pump operating point is calculated as follows. The system flow rate is fixed at Q_{sys}. The reference pressure, H_{ref}, is the pressure on the original pump curve that corresponds to this flow rate. This pressure and the known operating pressure from the system curve are used in Eq. 3.9 to calculate the speed of the new pump curve. This speed and the original pump speed are used to calculate the new operating power of the pump. The required net positive suction head (NPSHr) at the operating point is checked to ensure that it does not exceed the available NPSH (NPSHa). The NPSHa is calculated based on local atmospheric conditions, the suction pipe dimensions, and the height of the reservoir relative to the pump. Figure 3-6 shows an example pump selection where the original pump curve, calculated operating curve, and system operating point are shown.

The pumps are selected first for the case to ensure they can pump directly to the drip system, which means the volume of any tank paired with these pumps must be constrained such that the selected pump can fill it. In the event there is a tank

46
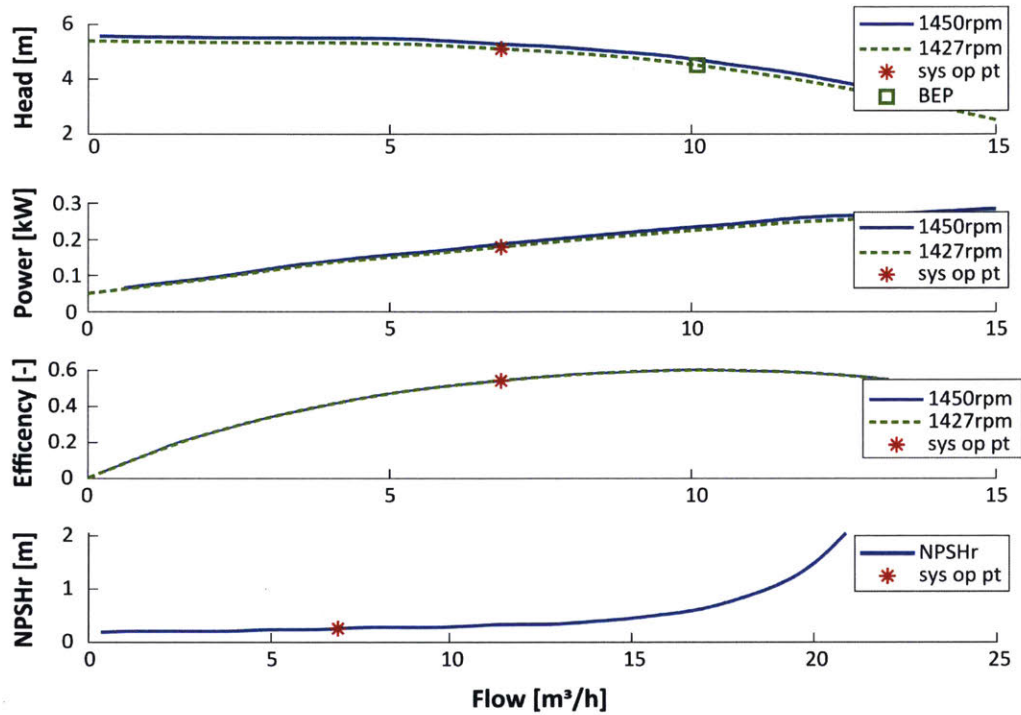
Figure 3-6: The constant system flow rate, Q_{sys}, is used to select a set of feasible pumps from a database such that the system flow rate is within 65-110% of the pump BEP flow rate. Each pump is assumed to be paired with a VFD. The system operating point (Q_{sys}, H_{sys}) is used along with the centrifugal pump affinity laws to determine the pump operating curve (dotted green line). The operating power, efficiency and NPSHr (red stars) can then be determined.

in the power system, the pump can operate at a range of flow rates and pressures because it is not constrained by the PC behavior of the hydraulic network. In order to simplify this calculation, the required head to pump to the tank is assumed to be fixed at half of the tank height. The tank is assumed to be elevated to a height in meters that is equal to the pressure loss in the hydraulic network, such that the tank can always pressurize the system. To reduce the height of the elevation stand, the tank is placed at the end of the main, just before the submain and laterals. This means that the required tank pumping head will always be greater than the system operating pressure. When the tank is less than halfway full, the fixed tank head is an overestimate of the pumping head required to pump to the tank, and when the tank is more than halfway full, the fixed tank head is an underestimate. In reality, the required pumping head will increase continuously as the tank fills and the flow rate to the tank will decrease, so this assumption is an average of sorts. This simplifies the calculation of the pump operating point when it pumps to a tank. As long as the ratio between the system pressure head in meters and the height of the tank is equal to or greater than two, this simplification results in, at most, a 15% error from the actual pumping power that is required to pump to the tank.

The calculation with the affinity laws for pumping to the tank is similar to that for the system operating point, but now the pumping head is fixed as the "known" value. Equations 3.8-3.10 can be used to parametrically plot the pump power as a function of head. The power on the original speed curve at P_{tank} is determined and used as P_{ref} (Figure 3-7a). The power available to the pump from the solar panels is known and used to determine the actual pump operating speed, N_{tank}. The equations are rearranged to calculate the power-head, power-flow, and pressure-flow pump curves at the actual operating speed. The actual power is used to determine the flow rate to the tank (Figure 3-7b). Finally, to check the calculation, the flow rate is used to find the pumping head on the pressure-flow curve at N_{tank}, which should be the assumed tank pumping head, P_{tank}. As shown in Figure 3-7c, that is indeed the case.

The benefit of doing this simulation for the tank is it allows the selected pump to fill the tank at a different flow rate from that of the drip system. Since the power
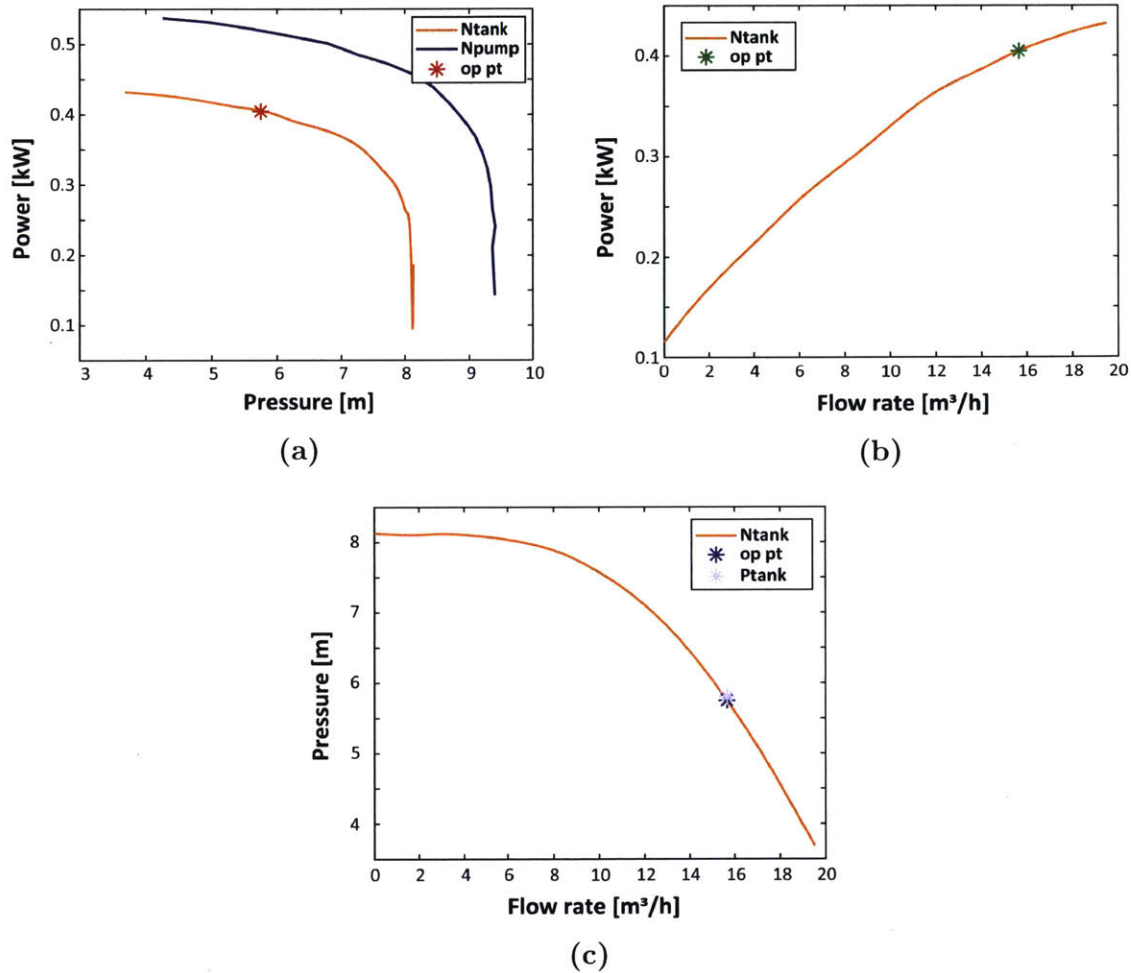
Figure 3-7: For designs that include a tank, the pump operation when pumping to the tank must be determined. A constant pumping pressure P_{tank} is assumed and used with the available power and affinity laws to determine the operating speed at each time step (red star). This is used to determine the flow rate to the tank (green star). The calculation can be checked by plotting the corresponding pressure on the pump pressure-flow curve, which should equal P_{tank} (blue stars). This simulation allows the flow rate to vary with available power when pumping to the tank.
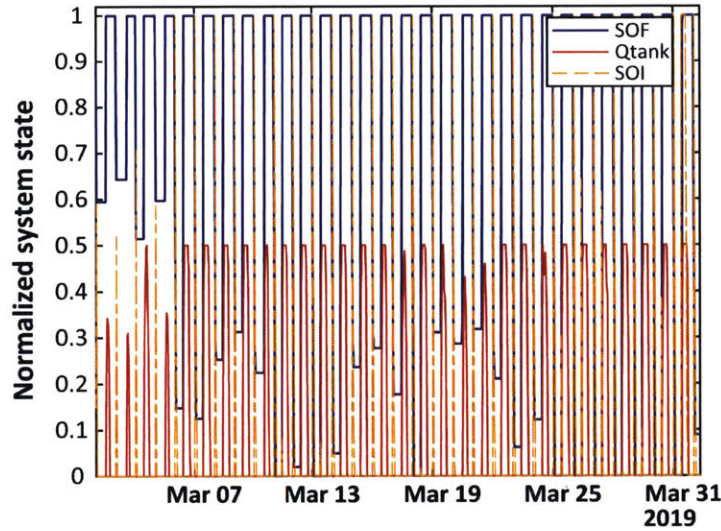
Figure 3-8: A snapshot of the simulated pump operation with a tank shows the pump can operate at various flow rates. This enables the system to store energy at times of low irradiance or after the irrigation demand has been met. The normalized tank SOF fills with Q_{tank} and drains during irrigation events (SOI).

consumption of the pump scales with the flow rate, this means the pump can store energy in the tank at times when the available power is too low to pump directly to the drip system, or take advantage of times when the field has been irrigated, but there is an abundance of solar power. A snapshot of this process is shown in Figure 3-8. The flow rate to the tank (Q_{tank}), SOF and the state of irrigation (SOI) are normalized for the sake of visualization. At the beginning of the month, an irrigation event occurs, shown by the SOI, followed by the pump filling the tank at a low flow rate. A similar pattern occurs on March 7th, but the pump fills the tank at a higher flow rate. The tank is able to fill and drain over a continuous range depending on the demand, available power and its previous SOF. The details of the energy distribution throughout the power system are discussed in the following section.

3.2.5 Power System Design & Operation

The power system module determines how much water a given system can deliver to the crops. It takes inputs from the agronomy, hydraulics, and pump modules, and it determines the solar panel area, battery capacity and tank volume. The power

system module computes an energy balance at each time step, Δt, to determine if there is enough power to run the system and deliver water to the crops. The default Δt is hourly, but can be modified based on the resolution of the weather data. The power system components each have associated operating limits, state vectors, and efficiencies. The battery cannot be drained past its maximum depth of discharge, which is set to 50% of its total capacity. The state vectors, SOC for the battery, SOF for the tank, and state of irrigation (SOI) in units of m^3, are defined at each Δt. The efficiency of the battery is assumed to be $\eta_{batt} = 85\%$, and the controller efficiency, η_c, is made up of the converter efficiency, $\eta_{conv} = 95\%$, and the MPPT efficiency, $\eta_{MPPT} = 98\%$. The solar panel efficiency varies with temperature and solar radiation, and can be computed in two ways in the model: an efficiency equation or a single diode model. Both assume a specific panel defined by datasheet parameters provided by the solar panel manufacturer. The panel used in this study was a Canadian Solar 270 Wp polycrystalline panel (Model number CS6P-270). The efficiency equation is simple and accounts for changes in temperature and solar radiation. Hourly irradiance and temperature data as well as constants from the panel datasheet are used to calculate the efficiency of the solar panels at each time interval, $\eta_{PV}(t)$ [35]:

$$\eta_{PV}(t) = \eta_{PV,nom} \cdot (1 + \alpha_P \cdot (T_{amb}(t) + k \cdot G_{solar}(t) - T_{std})) \qquad (3.11)$$

where $\eta_{PV,nom}$ is the nominal efficiency of the panels, α_P is the temperature co-efficient [%/$^\circ C$], and T_{std} is the standard testing temperature [$^\circ C$]. The ambient temperature, $T_{amb}(t)$, [$^\circ C$], and the solar radiation, $G_{solar}(t)$, [W/m^2], are taken from the local weather data. The Ross coefficient, k, relates irradiance to the PV module temperature ($k = 0.025^\circ Cm^2/W$). The PV power [W] at each time interval, $P_{PV}(t)$, is calculated in Equation 3.12, where A_{PV} is the panel area [m^2] for a given design.

$$P_{PV}(t) = \eta_{PV}(t) \cdot A_{PV} \cdot G_{solar}(t) \qquad (3.12)$$

The single-diode model, which is more exact and more computationally heavy compared to the efficiency equation (Eq. 3.11), is described in [25]. In this model, a

51
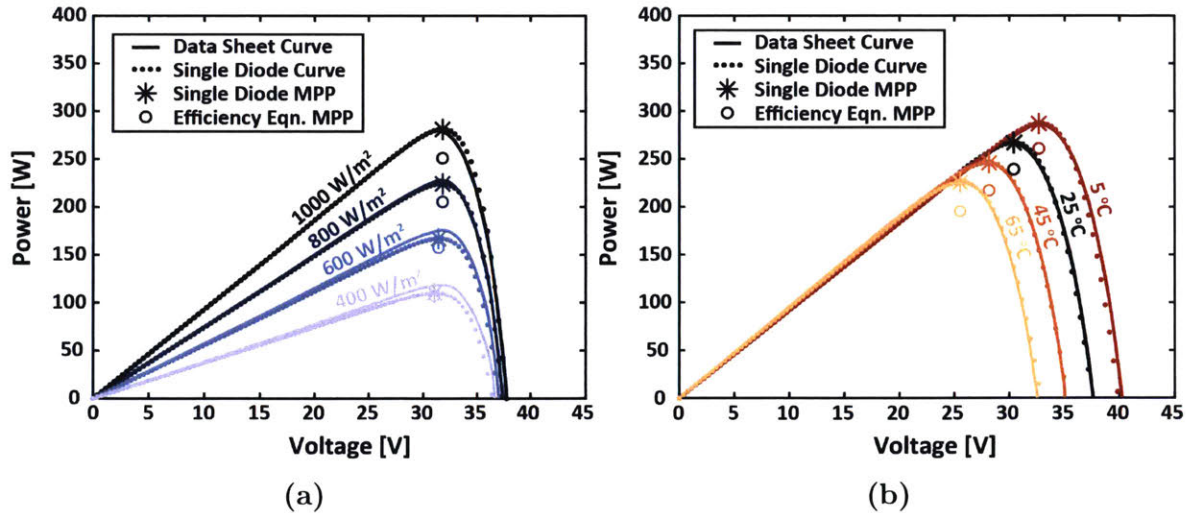
Figure 3-9: The single diode model is consistently more accurate in determining the power output of a PV panel at various irradiance levels (a) and temperatures (b) than the efficiency equation. However, the single diode model is more computationally expensive. Either may be used in the system model to predict the power output of the solar panels.

PV cell is represented by a single-diode equivalent circuit. The current-voltage curves are calculated from the model using parameters from the panel datasheet provided by the panel manufacturer. The maximum power point (MPP) can be found from the current-voltage curve. The curve and MPP change with solar radiation and temperature, so the calculation is repeated at each time step to produce the vector $P_{PV}(t)$.

Figure 3-9 shows that the single-diode calculation of the MPP is more accurate, with a maximum error 7.1% from the datasheet curve, compared to the efficiency equation MPP, which has a maximum error 14.6%. After $P_{PV}(t)$ is calculated, it is used to determine if there is enough power available at each time step to deliver water through the hydraulic system to the crops.

For each proposed power system design, the system model simulates its operation over the course of a growing season. There are four different energy pathways that can be taken to deliver water to the crops and two pathways to store energy. These six pathways are considered in a loop within the power system module and are illustrated in Figure 3-10.

52
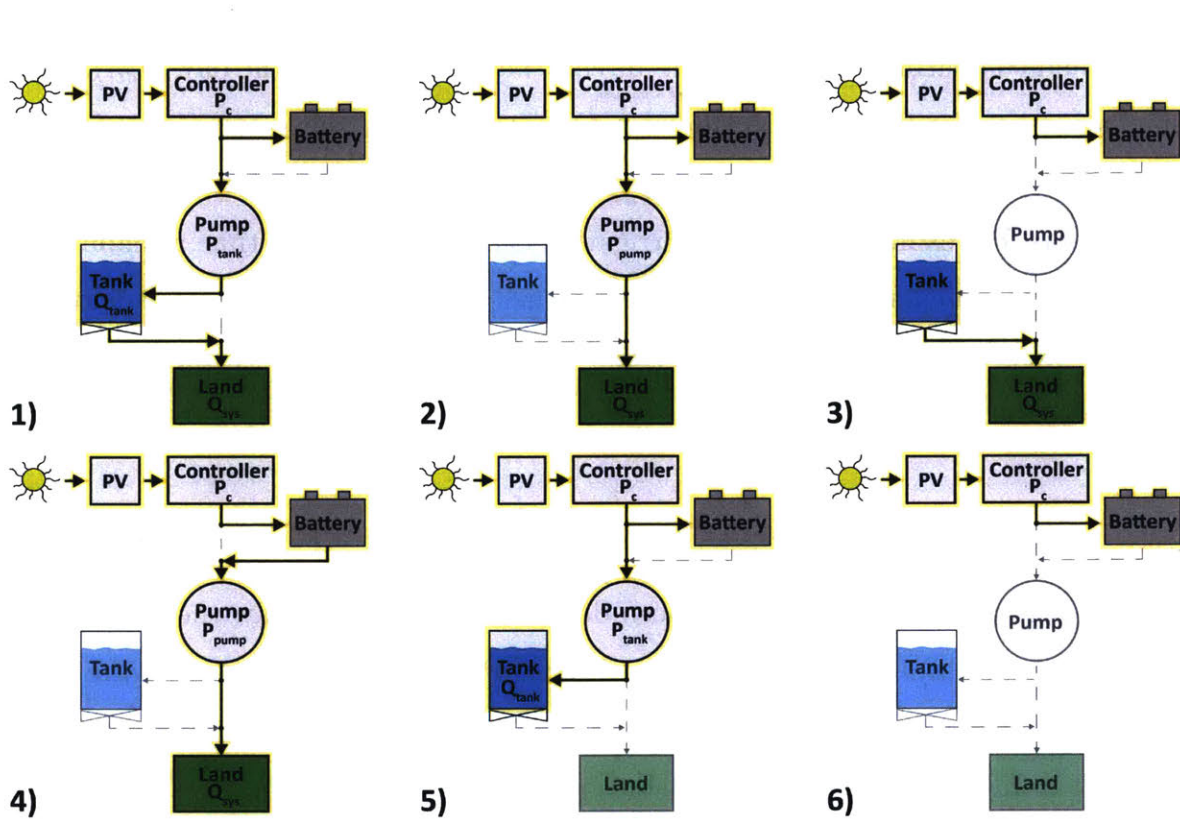
Figure 3-10: The system operation simulation has six possible pathways, with four that power the system and two that store energy. (1) fills the tank and delivers water to the field. (2) pumps directly to the field and (3) drains the tank to the field. Pathways (1)-(3) also charge the battery when there is enough power. (4) charges the battery and uses it to power pumping directly to the field. (5) charges the battery and fills the tank, and (6) just charges the battery. These pathways are tested in sequence to determine which can be used, and multiple pathways may be used in a given time step. This sequence is fixed and prioritizes irrigating over storing energy.

The controller efficiency is applied to $P_{PV}(t)$ to determine the actual power available to the drip system:

$$P_c(t) = \eta_c \cdot P_{PV}(t).$$

(3.13)

The power system loop starts by calculating the irrigation demand, I_{dem} (Section 3.2.6), and comparing this to what has already been delivered for the day, (I_{del}). This simulation has the flexibility to run multiple pathways in a single time step. It does this by keeping track of the time it takes to achieve certain tasks during a time step in the loop. For example, before the irrigation demand is met, the time remaining to irrigate, t_{ri}, is calculated (Eq. 3.14). This ensures that the amount of water delivered will not exceed the daily demand and that, if the demand is met within the current time step, the remaining time can be spent in a different pathway.

$$t_{ri} = min(\frac{I_{dem} - I_{del}}{Q_{sys}}, \Delta t)$$

(3.14)

If I_{dem} is greater than what has been delivered so far for the day, then the power system loop checks if it can deliver water through Pathway 1, as shown in Figure 3-10. Pathway 1 fills the tank and delivers water at the same time. During this pathway, the time to fill the tank, t_{tf}, is calculated by Equation 3.15.

$$t_{tf} = min(\frac{C_{tank} - SOF(t - 1)}{Q_{tank}(t) - Q_{sys}}, t_{ri})$$

(3.15)

The t_{tf} calculation ensures that the tank will not exceed its capacity, C_{tank}, and that other pathways can be run once the tank is full. For Pathway 1 there must be enough power to pump to the tank ($P_c \geq P_{tank}$) and the tank should be filling ($Q_{tank} > Q_{sys}$). The state vector equations for this pathway are Equations 3.16-3.18. Figure 3-11 shows an example of the power system operation over two days with the sequence of pathways from Figure 3-10 labeled. Pathway 1 occurs during day two, hour ten, when SOI is greater than zero, SOF increases, and SOC is at its maximum.

$$SOI(t) = Q_{sys} \cdot t_{ri}$$

(3.16)

54
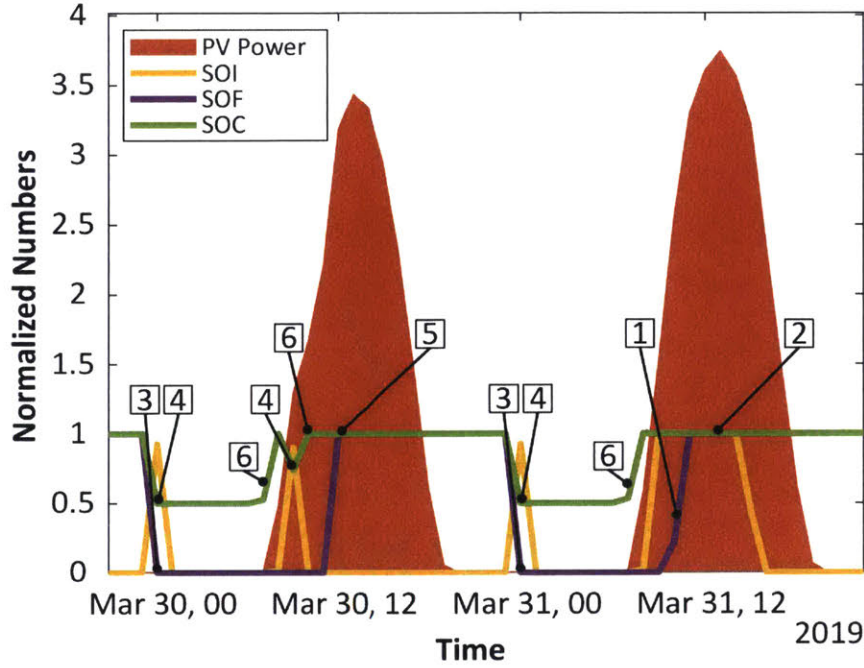
Figure 3-11: An example of how the logic flow determines the system state over two days. The available solar power (orange) is shown for reference. On March 30th, the system irrigates by first draining the tank, then powering the pump with the battery (3,4). The battery is charged, drained and charged over the course of an irrigation event (6,4,6). The tank is filled using excess power (5). March 31st begins like the previous day, but after sunrise, it fills both the tank and battery and irrigates using direct drive (1,2) because there is more power available on this day.

$$SOF(t) = SOF(t-1) + (Q_{tank}(t) - Q_{sys}) \cdot t_{tf} \qquad (3.17)$$

$$SOC(t) = SOC(t-1) + (P_c(t) - P_{tank}(t)) \cdot t_{tf} \qquad (3.18)$$

If there is not enough power to complete Pathway 1, the loop checks if there is enough power to deliver water through Pathway 2 (Figure3-10). This pathway delivers water directly from the pump, so there must be enough power to run the pump ($P_c \geq P_{pump}$). The state vector equations for this pathway are Equations 3.16, 3.19 and, 3.20. This is shown in Figure 3-11 on day two, hour 12, with an SOI greater than zero, a constant SOF, and SOC at its maximum.

$$SOF(t) = SOF(t-1) \qquad (3.19)$$

55

$$SOC(t) = SOC(t-1) + (P_c(t) - P_{pump}) \cdot t_{ri} \qquad (3.20)$$

If there is not enough power for Pathway 1 or 2, there is not enough power from the panels to directly deliver water, so the loop checks if there is enough energy storage to power irrigation. The two storage options are the tank and the battery, so it calculates how long it would take to first drain the tank and then drain the battery with Equations 3.21 and 3.22. Note that if the tank or battery are already at their minimum then t_{td} and t_{tdb} are zero.

$$t_{td} = min(\frac{(0 - SOF(t-1))}{Q_{tank}(t) - Q_{sys}}, t_{ri}) \qquad (3.21)$$

$$t_{tdb} = min(\frac{0.5 \cdot C_{batt} - SOC(t-1)}{P_c(t) - P_{pump}/\eta_{batt}}, t_{ri}) \qquad (3.22)$$

The power system loop then uses Pathway 3 to drain the tank and irrigate through the pipe network. Using the t_{td} calculation ensures that the tank is not drained past its minimum, which is physically impossible. The state vector equations for this pathway are Equations 3.23-3.25. This is shown in Figure 3-11 on hour zero of days one and two, with a *SOI* greater than zero and a *SOF* drained to zero.

$$SOI(t) = Q_{sys} \cdot t_{td} \qquad (3.23)$$

$$SOF(t) = SOF(t-1) - Q_{sys} \cdot t_{td} \qquad (3.24)$$

$$SOC(t) = SOC(t-1) + P_c(t) \cdot t_{td} \qquad (3.25)$$

If Pathways 1 to 3 have been fulfilled for a time step, the power system loop checks if water can be delivered through Pathway 4. This pathway powers irrigation with the energy stored in the battery, so using the t_{tdb} calculation (Eq. 3.22), ensures that the battery is not drained past its set depth of discharge, 50%. The state vector equations for this pathway are Equations 3.26, 3.19 and 3.27. This is shown in Figure 3-11 at hour zero of days one and two and hour nine of day one with an SOI greater than zero and drained SOC. Hour nine of day one has a smaller draining of SOC compared to hour zero for the same irrigation amount. This is because solar power

is available in hour nine, so the battery is charging and draining at the same time.

$$SOI(t) = Q_{sys} \cdot t_{tdb} \tag{3.26}$$

$$SOC(t) = SOC(t-1) + (P_c(t) - P_{pump}/\eta_{batt}) \cdot t_{tdb} \tag{3.27}$$

Next, if there is not enough power or energy storage to run the other pathways, or the irrigation demand for the day has been met, the SOI is set to zero. Then, the loop checks if the tank and battery are full, and if not, it tries to fill them using Pathways 5 and 6. For Pathway 5, the t_{tf} is updated by setting Q_{sys} to zero with Equation 3.28. The SOF and SOC are calculated with Equations 3.29 and 3.30. Pathway 5 is shown in Figure 3-11 at day one hour 12, after the demand has been met, with SOI at zero and SOF full.

$$t_{tf} = min(\frac{C_{tank} - SOF(t-1)}{Q_{tank}(t)}, \Delta t) \tag{3.28}$$

$$SOF(t) = SOF(t-1) + Q_{tank} \cdot t_{tf} \tag{3.29}$$

$$SOC(t) = SOC(t-1) + (P_c(t) - P_{tank}) \cdot t_{tf} \tag{3.30}$$

Finally, after trying to fill the tank, the system uses any remaining power to charge the battery through Pathway 6. The state vector equations are Equations 3.19 and 3.31.

$$SOC(t) = SOC(t-1) + P_c(t) \cdot \Delta t \tag{3.31}$$

Note that a time to charge the battery is not calculated because any extra power is always used to charge the battery. The battery is always set to have a maximum limit of C_{batt} when it is charging. If there is any extra power after the battery is fully charged, it is unused. Pathway 6 is shown in Figure 3-11 on day one, hour eight and ten, and on day two, hour eight with SOI at zero and SOF increasing or full. This pathway happens when the demand has not been met, but there is very little PV power, or after the demand is met. At the end of each time step, the total daily water

that was delivered to the field, (I_{del}), is calculated by summing the SOI vector. The vector of daily water delivered is saved to later be compared to the daily demand, I_{dem}.

There are a few additional aspects of Figure 3-11 that are interesting to note. The tank and battery are filled by the end of the day, but immediately drained at the start of the next day. This is because the power system model is set to try to reach the water demand starting at hour zero of each day by default. Pathway 3 and 4 also occur at the same time at hour zero of each day. This is because the tank was not set to be large enough to deliver water for the entire Δt by itself. Finally ,the SOI in day one is only greater than zero for two time steps, but the SOI in day two is greater than zero for much longer. This is because the water demand in day one is less than the demand in day two.

The simulation of the energy flow through the power system allows for an accurate assessment of the performance of a particular design. Although the operation scheme is fixed by the predetermined sequence of the pathways, it is a reasonable model of how a system could operate in the field. In future iterations of the model, the operation scheme itself will be optimized. The most important output of the power system module is the water delivered throughout the season, which is directly used to determine the reliability of the system design.

3.2.6 Crop Yield

The crop yield module takes the weather data, crop parameters, soil properties, and water delivered by the given system design as inputs, and uses these to calculate the crop yield for the season. In literature, it has been shown that irrigating less, or practicing deficit irrigation, can lead to water savings with low impact on, or even benefits to, yield production [10, 23]. Simulating the impact of deficit irrigation on crops can allow for smaller, less expensive systems that meet less of the crop water demand.

The crop water demand is calculated using the soil water balance method for water stress conditions [29]. Figure 3-12 illustrates the water balance of the root

58
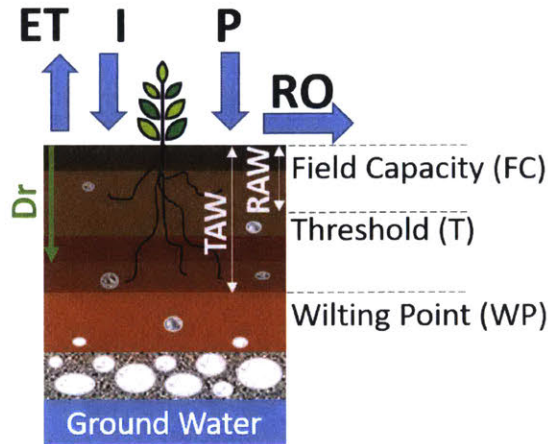
Figure 3-12: The soil water balance at the crop root zone depends on the evapotranspiration (ET), irrigation (I), precipitation (P), and root zone depletion (D_r), which is dictated by the readily available water (RAW) and total available water (TAW). Accounting for these parameters on a daily basis allows for a more accurate calculation of the irrigation demand and thus a more finely tuned system design.

zone. The field capacity (FC) is the total amount of water that the soil can hold. The wilting point (WP) is the amount of water in the soil that will cause the plant to permanently wilt. The FC and WP are determined by the soil texture, which is based off of the soil texture triangle [36]. The precipitation, P, comes from the weather data. The total available water (TAW) in the root zone of the plant is the difference between the FC and WP. The TAW is the amount of water that the plant can extract from the soil. This depends on the depth of the roots, which is taken from the crop database. The readily available water (RAW) is the amount of water in the root zone that the plant can uptake most efficiently. The RAW is the threshold below which the plant begins to feel water stress. The TAW is multiplied by a depletion fraction, p, to get the RAW. The factor p depends on the crop and is adjusted for ET_c using

$$p(t) = p_{const} + 0.04 \cdot (5 - ET_c(t)), \tag{3.32}$$

where p_{const} is the constant crop dependant depletion fraction averaged over the growth stages of the crop.

The root zone depletion, D_r, is the water lost in the root zone of the plant. When D_r goes below RAW, the plant begins to feel water stress. The D_r is calculated using the soil water balance in Equation 3.33. It should be noted that for this balance it is assumed that the groundwater table is sufficiently far enough away from the root zone that there is no capillary rise. Furthermore, there are limits on D_r (Eq. 3.34), such that if over irrigation or a heavy rain occurs, water is lost due to deep percolation and D_r becomes zero. If the crops receive no water, the maximum D_r is TAW.

$$D_r(t) = D_r(t-1) - P(t) + RO(t) - I_{del}(t) + ET_{c,adj} \tag{3.33}$$

$$0 \leq D_r(t) \leq TAW \tag{3.34}$$

In the above equations, P is the precipitation in mm. The runoff, RO, in mm, is a fraction of P based off of the soil texture [37]. I_{del} is calculated in the power system module and converted to mm using Equation 3.4. The crop evapotranspiration adjusted for water stress, $ET_{c,adj}$, is:

$$ET_{c,adj}(t) = K_s(t) \cdot ET_c(t). \tag{3.35}$$

The water stress coefficient, K_s, is determined by D_r. If D_r is less than or equal to RAW, then K_s is one. If the D_r is greater than RAW, then K_s is described by:

$$K_s(t) = \frac{TAW - D_r(t)}{(1 - p(t))TAW}. \tag{3.36}$$

In the power system module, the irrigation demand is calculated at the start of a day by first rearranging Equation 3.33 to solve for I_{del} and then setting $ET_{c,adj}$ to ET_c and D_r to RAW, as seen in Equation 3.37. This assumes that the depletion is at RAW and water stress does not occur. Note the initial D_r is set to RAW.

$$I_{dem}(t) = D_r(t-1) - P(t) + RO(t) - RAW(t) + ET_c(t) \tag{3.37}$$

Then, in the power system module, I_{del} and D_r are calculated at the end of the day, such that D_r can be used to solve for the irrigation demand at the start of the

next day. Since $ET_{c,adj}$ depends on D_r through K_s, Equation 3.33 must be combined with equations 3.35 and 3.36 to solve directly for D_r with Equations 3.38 and 3.39.

$$D_r(t) = D_r(t-1) - P(t) + RO(t) - I_{del}(t) + \frac{TAW - D_r(t)}{(1 - p(t))TAW} ET_c(t) \qquad (3.38)$$

$$D_r(t) = \frac{D_r(t-1) - P(t) + RO(t) - I_{del}(t) + \frac{TAW \cdot ET_c(t)}{(1-p(t))TAW}}{1 + \frac{ET_c(t)}{(1-p(t))TAW}} \qquad (3.39)$$

It should be noted that currently the factor p is computed as an average for each growth stage of the crop. This is the reason for the spikes in water demand in Figure 3-2, as between growth stages there is a sudden change in p, which leads to a sudden change in water demand.

After the $ET_{c,adj}$ is calculated, the yield can be calculated by relating a reduction in evapotranspiration to a reduction in yield [8]:

$$1 - \frac{Y_a}{Y_{max}} = K_y(t) \cdot (1 - \frac{ET_{c,adj}(t)}{ET_c(t)}), \qquad (3.40)$$

where Y_{max} is the maximum yield and K_y is the crop yield response factor [8].

This is a linear approximation of change in yield to change in evapotranspiration. In reality, the actual yield calculation is much more complex, but this is a good first approximation. The crop yield response factor, K_y, varies by crop and can also change depending on the development stage of the crop, similar to K_c. In the yield module, K_y is an empirically determined value from the crop database [8]. The maximum yield, Y_{max}, refers to the maximum yield that a crop can achieve assuming it experiences no water stress, fertilizer stress, soil salinity and acidity, and pest conditions. Y_{max} is calculated using code based on the agro-ecological zone method [8]. In this method the gross dry matter for a standard crop is calculated for given local weather data. Then this is multiplied by correction factors for species and temperature, crop development, net dry matter production, and the harvested part of the plant. The yield calculated from this process, Y_{max}, can be seen as a potential yield that gives an indication of the agricultural production efficiency, but
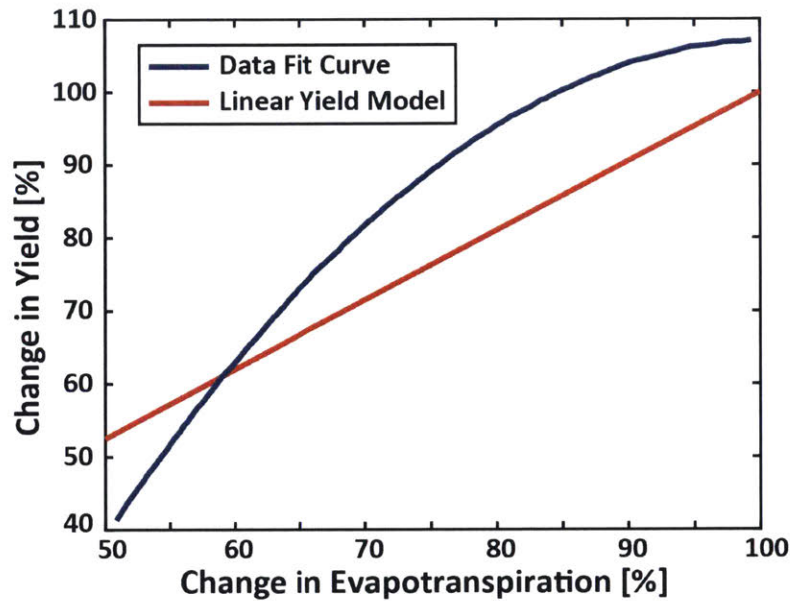
Figure 3-13: The linear and data fit yield curves for olives show the percent change in yield as a function of the change in crop evapotranspiration (ET), which is related to crop water demand. The fit curve more accurately characterizes the resistance of olives to water stress for low changes in ET. Below 50% ET it is assumed the yield falls to zero.

is not necessarily the exact yield that would be measured in the field.

A large problem with the linear crop yield approximation is its dependence on an empirically derived factor. K_y has been shown to vary widely between studies, even for the same crop variety [10]. Therefore, the yield module was built with the capability to use the linear yield approximation or a crop specific change in evapotranspiration versus change in yield curve to calculate the actual yield, Y_a. The difference between the two curves is shown in Figure 3-13 for olives.

In Figure 3-13 it can be seen that the nonlinear curve more accurately depicts the drought resistant nature of the olive crop as it stays at or above 100% yield for greater than 85% evapotranspiration. The linear yield model is more conservative and assumes 100% yield is only possible with 100% evapotranspiration. The nonlinear curve does not have data for evapotranspiration below 50%, therefore when using the nonlinear curve to predict yield in the system model, it is assumed that the yield is zero below 50% evapotranspiration. Because many studies have shown that declines in yield are not noticeable for small reductions in evapotranspiration for olives, the

nonlinear curve is used for the olive yield calculation in this model. An important feature of the yield module is that it allows for the performance of a design to be evaluated based on its generated crop revenue.

3.3 Model Functionality

3.3.1 Optimization Formulation

As described at the beginning of Section 3, the PSO algorithm generates possible designs and sets the trajectory of the design vector. The objective of the optimization can either minimize life cycle cost or maximize profit. In addition, a reliability constraint is imposed on the optimization to ensure some amount of water delivery and therefore crop yield. A PSO randomly generates an initial set of solutions to the optimization problem, which is called the initial swarm. These solution vectors are permutations of the design variable values. Each solution is run through the model, and the performance of each solution vector is determined by the objective function value it produces, in this case either a system cost or profit. Depending on the problem formulation, whichever solution minimizes or maximizes the objective function value is identified as the best performing solution of its swarm. The PSO then updates the swarm using parameters that determine the "velocity" of the particles within the design space. The process of establishing a swarm, testing each solution in the model, selecting the best solution and then shifting the swarm within the design space based on the result is repeated until the algorithm converges on a solution [38]. The swarm velocity parameters and convergence criterion can be altered to change the speed and accuracy with which the optimization converges on an optimum. There is no way to guarantee that a heuristic optimization method has reached a global optimum, but if it converges to the same solution repeatedly, this is a good indication that the solution is an optimum [38].

The PSO method was chosen because it is a heuristic method that allows for discrete variables and discontinuous functions. It also tends to be less computationally

expensive than genetic algorithms [38]. In this model, the continuous design variables are the capacities of the panel array, the tank, and the battery. The only discontinuous design variable is the pump, but the pump variable vector is arranged in order of increasing maximum operating power, so that there is some directionality to the pump selection. To ensure that the selected pumps can operate as described in Section 3.2.4, the maximum allowable tank volume is constrained by the selected pump performance capabilities. The main constraint imposed on the optimization is a reliability requirement, which forces the system to meet at least 85% of its hydraulic load on average over the course of the growing season. The modules described in the proceeding sections that simulate the system behavior contain a number of functions that are non-linear with respect to the optimization design variables. Therefore, this is a constrained, non-linear optimization problem with discrete variables.

3.3.2 Objective Function

The objective function is based on the system cost. There are several examples in literature of life cycle cost equations for solar powered pumping and irrigation systems. Oclan (2015), Campana (2015), Campana (2016), and Lopez (2015) use interest rate for their net present value life cycle cost calculations, while Mohammadi (2015), Niajalili (2017), and Muhsen (2017) include inflation as well as interest rate [39, 40, 41, 23, 42, 43, 20]. The calculations for the maintenance and replacement costs of components in the system are included, either by calculating separate cost numbers [39, 41, 42, 20] or by lumping them together [40]. Many calculated a reliability factor, called the loss of load probability (LLP), either as a function of energy used [39], or as a function of water delivered [42, 20]. Most of the cost equations used in this study are modified from [20], as it was found to be the most comprehensive model that incorporated maintenance, replacement, and initial capital cost with net present value calculations that included inflation and interest rates.

The two possible objectives for the optimization are to minimize life cycle cost, LCC, or to maximize profit, as shown in Equation 3.41. The two different objectives allow the user to either optimize for the lowest cost system with a minimum reliability

constraint, or to optimize with no reliability constraint, and to instead include a measure of system reliability in the objective itself by calculating the yield. Profit is calculated as the revenue earned from crop yield over the lifetime of the system minus the LCC. The present value of the revenue earned from the crop yield is calculated in Equation 3.42. The unit crop prices (k_{cp}) were found from producer prices based on the specified country and the most current year available [44]. In equation 3.42, the present value is calculated with inf as the inflation rate, i as the interest rate, and LT as the lifetime of the system. Note that inf and i will change based on the country and year being analyzed.

$$F = \begin{cases} min(LCC) \\ \\ or \\ \\ max(Profit) = max(Rev - LCC) \end{cases} \tag{3.41}$$

$$Rev = \begin{cases} Y_a \cdot A_{field}/10000 \cdot k_{cp}\left(\frac{1+inf}{i-inf}\right)\left(1 - \left(\frac{1+inf}{1+i}\right)^{LT}\right) & if \ i \neq inf \\ Y_a \cdot A_{field}/10000 \cdot k_{cp} \cdot LT & if \ i = inf \end{cases} \tag{3.42}$$

The life cycle cost is a sum of the initial cost (IC), the maintenance cost (MC), and the replacement cost (RC) for the lifetime of the system:

$$LCC = IC + MC + RC. \tag{3.43}$$

The IC is calculated as the sum of the initial capital costs (IC_n) of each component in the system plus the installation cost (ICI):

$$IC = \sum_{n=1}^{N} IC_n + ICI. \tag{3.44}$$

There are five component costs considered in the system: the pump, the hydraulic network, the panels, the battery, and the tank. The price of the tank stand scales with the operating pressure of the hydraulic network and is included with the tank

65

cost. The pump capital cost is taken from the pump database and, at the moment, the controller cost is lumped in with the pump cost. For the cases that the pump cost was unknown, the capital cost was assumed to scale with the maximum power of the pump,

$$IC_{pump} = UC_{pump} \cdot C_{pump}.$$ (3.45)

where UC_{pump} is the assumed pump unit cost in $\frac{USD}{kW}$ and C_{pump} is the pump capacity in kW. The hydraulic network capital cost is calculated based on a unit cost for a hydraulic system (UC_{hyd}), that is scaled with the field area, then added to the online emitter cost.

$$IC_{hyd} = UC_{hyd} \cdot A_{field} + UC_{emit} \cdot N_{emit}$$ (3.46)

UC_{emit} is the unit cost of the emitters and N_{emit} is the total number of emitters in the system. The PV panel, battery, and tank capital costs are calculated based on a unit cost, UC_n, and then scaled based on their respective capacities, C_n.

$$IC_n = UC_n \cdot C_n$$ (3.47)

It should be noted that the unit cost of the PV panels includes the cost of their frames and stands. The ICI is assumed to be a fraction, k_i, of the total initial capital cost of the system.

$$ICI = k_i \sum_{n=1}^{N} IC_n$$ (3.48)

The MC is calculated as the sum of the maintenance costs each component MC_n. The MC_n is calculated as a present value:

$$MC = \sum_{n=1}^{N} MC_n,$$ (3.49)

where

$$MC_n = \begin{cases} MC_{0n}\left(\frac{1+inf}{i-inf}\right)\left(1-\left(\frac{1+inf}{1+i}\right)^{LT}\right) & if \ \ i \neq inf \\ MC_{0n} \cdot LT & if \ \ i = inf. \end{cases}$$ (3.50)

In Equation 3.50, MC_{0n} is the maintenance cost of the nth component for the first year. The MC_{0n} is assumed to be a fraction (k_m) of the initial capital cost of the nth component.

$$MC_{0n} = k_m \cdot IC_n$$ (3.51)

The replacement cost is calculated as a present value with

$$RC_k = IC_k \sum_{j=1}^{N_r} \left(\frac{1+inf}{i-inf}\right)^{\frac{LT \cdot j}{N_r+1}},$$ (3.52)

where RC_k is the replacement cost of the components that need to be replaced k times over the lifetime of the system, and IC_k is the initial capital cost of the components that need to be replaced. The sum of all the individual component replacement costs is the total replacement cost,

$$RC = \sum_k RC_k,$$ (3.53)

where N_r is the number of replacements that a component will need over the lifetime of the system, which depends on the components lifetime, LT_n.

$$N_r = floor\left(\frac{2LT-1}{2LT_n}\right)$$ (3.54)

A caveat to this is that two system components only have a partial replacement over the system's lifetime. First, only 10% of the panels are "replaced" every ten years to represent panel degradation over time. Additionally, for the hydraulics system, only the laterals and emitters need to be replaced every ten years.

It should be noted that all of the economic data used was calculated based on

values found while conducting field trials in Morocco and Jordan (Section 5). Each of the values were based on prices from local contractors and economic reports conducted by local agricultural research institutions [15, 16]. The raw data were converted to a unit price and scaled based on the system size being analyzed. The values used for each country are listed in Appendix A.

3.3.3 Reliability Metric & Objective Flexibility

The main constraint in this optimization problem is the reliability metric. This metric exists in different forms for the cost-minimization and profit-maximization versions of the problem. When the objective is to minimize the life cycle cost of the system, the loss of load probability (LLP) is constrained. The LLP is defined in Equation 3.55 as the difference between the total water demand over the irrigation season, Q_{demand}, and the total water delivered by the system, $Q_{delivered}$, divided by the total water demand. This number represents the average probability that the daily water requirement will not be met. The larger the LLP, the lower the reliability of the drip system design. For the cost optimization problem, a maximum LLP of 0.15 is set, ensuring that every design must on average meet the water demand 85% of the time. This is a maximum, so some designs may be more reliable, with a lower LLP, if the lowest cost system can meet more of the demand. This LLP limit is set based on the nonlinear olive yield curve, which shows that at 85% evapotranspiration, 100% yield is achievable (Section 3.2.6).

$$LLP = \frac{\sum Q_{demand} - \sum Q_{delivered}}{\sum Q_{demand}} \tag{3.55}$$

When the objective is to maximize the lifetime profit of the system, the crop yield module becomes a part of the model. This module calculates the crop yield based on the water delivered during the season, and the yield translates directly to revenue. Although LLP is not capped, the reliability of the system is constrained because the crop yield creates a relationship between the water delivered by the system and the profit. The more reliable the system, the higher the profits. It is

68

important to have both a cost and profit optimization because the profit tends to be at least an order of magnitude larger than the system cost. This means that the cost optimization is more sensitive to small changes in the design variable capacities because the component costs are closer in magnitude to the value of the objective function. However, optimizing for profit allows for the use of the crop yield module, which acts as a more generalizable constraint on the system reliability.

Chapter 4

Simulation Results

4.1 Simulation Sample Case

The sensitivity and robustness of the optimization is explored in a series of simulated experiments with various parameters. The sample case used in these simulations is an olive grove in Morocco with low-pressure, online PC emitters. The trees have a 5 m by 5 m spacing and there are two emitters at each crop. Unless otherwise stated, the field is 1 ha and the emitters have a rated flow rate of 8 Lph and an activation pressure of 0.15 bar. These simulations are used to explore the design space, identify the limitations of the model in its current configuration, and justify the selection of optimization parameters and constraint values. For the sample case, it is shown that the optimization produces a direct drive system, or a system with only solar panels, that is 62% cheaper than the solution produced by the conventional design method for drip irrigation systems.

The conventional way to size a drip irrigation system involves a set of calculations based on average weather data and simplifying assumptions about the selected components. This method is based on conversations with irrigation engineers in Jordan and Morocco and the Lorentz Compass tool, a commercially available software that sizes solar powered pumping systems. The system operating point produced by the hydraulic module for the sample case can be used to start: 6.9 m^3/h at 5 m head. Equation 4.1 can be used to calculate the hydraulic power to be 0.096 kW. If a pump

efficiency of 40% is assumed, the power the pump requires from the panel array is 0.24 kW. If the controller electronics are assumed to have a combined efficiency of 95% and the panel efficiency is assumed to be a constant 16%, then the total power required by the panels is 1.6 kW (Eq. 4.2). It should be noted that the assumed efficiencies are generous, and in the case of the panels, the efficiency is assumed to be independent of available irradiance and temperature.

$$P_{hyd} = \frac{Q_{sys}}{3600} \times H_{sys} \times 1000 \times 9.81 \qquad (4.1)$$

$$P_{PV} = \frac{P_{hyd}}{\eta_{pump}\eta_c\eta_{PV}} \qquad (4.2)$$

The olive irrigation season is the beginning of March to the end of November. The month with the lowest average irradiance is November, with 300 W/m^2 according to TMY weather data for Morocco [30]. Equation 4.3 can be used to calculate that the system would required a panel area of 5.3 m^2 to operate throughout the growing season. This will be the comparison point for the optimized sample case system design.

$$A_{PV} = \frac{P_{PV}}{min(G_{sun,avg})} \qquad (4.3)$$

4.2 Sensitivity Analysis

For the sample 1 ha case, the Pareto front of life cycle cost and panel area is used to understand how the composition of the design impacted the cost. The optimal emitter flow rate is determined for a range of field sizes to explore the possibility of using the model to inform emitter design. Finally, the model sensitivity to the reliability requirement is explored by both changing the maximum allowed LLP for several field sizes in the cost optimization and running the profit optimization, which includes the crop yield module, for a range of field sizes. The result of these simulations justify an LLP limit of 0.15 and show that the optimal design for smallholder farms - farms of

72
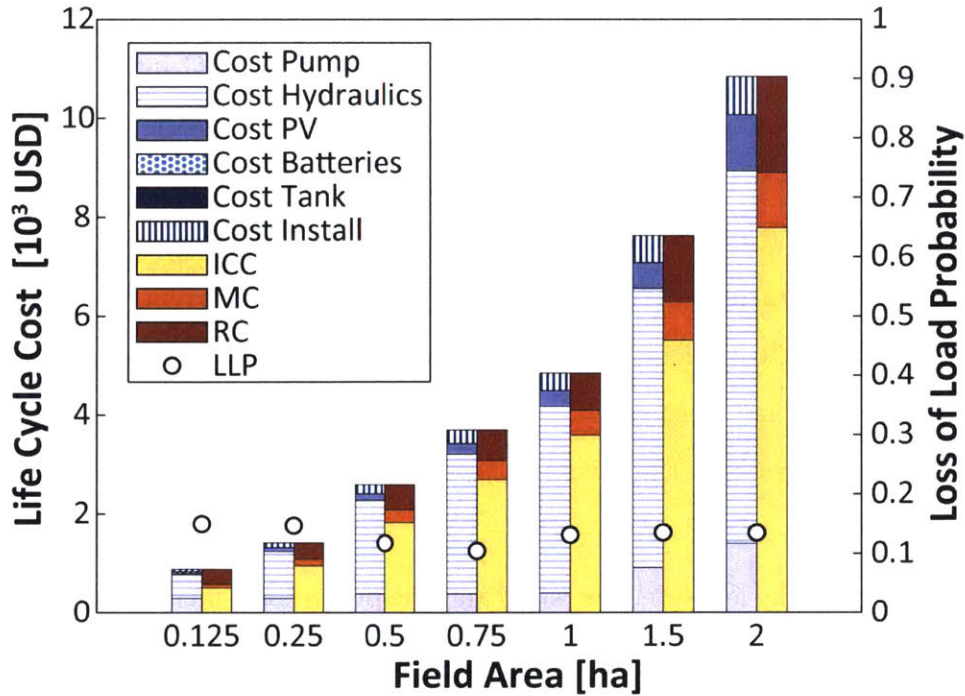
Figure 4-1: The sensitivity of the optimum life cycle cost (LCC) to field size. The systems are direct drive or have a small energy storage capacity. The bar on the left breaks down the LCC into component costs, showing that the hydraulic network makes up over 50% of the cost in all cases. The bar on the right breaks down the LCC into initial, maintenance, and replacement costs, showing that the initial cost makes up more than 70% of the cost in most cases. The loss of load probability (LLP) hovers between 0.1 and 0.15, reaching a minimum in the 0.75 ha case.

2 ha or less - is a direct drive system with an emitter flow rate between 2 to 6 Lph, depending on the size of the field. The results also show that the initial cost of the system is by far the majority of the life cycle cost, between 57-74%, indicating subsidy programs that cover the initial investment could significantly reduce the adoption barrier for smallholder farmers.

The sensitivity of the life cycle cost to changes in field area with the corresponding cost breakdown is shown in Figure 4-1. This analysis is conducted by optimizing for the minimum life cycle cost system design for seven field sizes from 0.125 to 2 ha. All remaining input case parameters were equivalent to the sample case except the field area. The resulting life cycle cost (LCC) and loss of load probability (LLP) for the optimal designs are plotted against field area. The optimal designs obtained from this analysis are shown in Table 4.1.

Figure 4-1 plots two representations of LCC per field area. The left side splits the LCC into its component costs, while the right side splits LCC into initial, maintenance, and replacement costs. The hydraulic network is the most expensive component in the system over this range of field areas. In fact, the hydraulics make up more than 50% of the total life cycle cost for each field area, and up to 78% of the total LCC for the one hectare case. The hydraulic network is not currently cost-optimized, but it is important to understand the relative scale of the component costs. The hydraulic network costs were compared to contractor prices in Jordan and Morocco for similarly sized systems that were compiled for the field trials and found to be reasonable.

Additionally on the left side, the panel and the pump costs increase as the field area increases because the hydraulic load of the system scales with field area. The pump operating point also changes with the field layout. Table 4.1 shows how the pump power and panel area increases with field area. The 0.5 ha and 0.75 ha cases have optimal designs with the same pump, but the larger field has a higher pump power because it has a higher system operating point. The 0.125 and 0.25 ha cases have optimal designs with different pumps of the same size, meaning they have optimal designs with the same pump cost (Eq. 3.45) but different pumps and operating points.

Interestingly, there is very little energy storage for the field sizes analyzed, and most of the optimal designs can be seen as direct drive systems. For the designs that do included energy storage options, the capacities, and therefore costs, are so small that they cannot be seen in Figure 4-1. The only design that includes batteries is for the 0.125 ha field, and it is a small battery, with approximately the same capacity as five rechargeable AA batteries. Batteries are not optimal for smallholder farms most likely because of their high replacement cost. The 1 ha case has a tank, but this tank is approximately one gallon and only makes up 0.01% of the total LCC. Therefore, this tank is an artifact of the optimization, and realistically the design would not include a tank. Tanks are not an optimum because of their high unit cost, and because they are limited in size by the pump, they will not become viable until larger pumps are selected.

Table 4.1: Optimum LCC Design for Various Field Sizes

Field Size [ha]	Pump No.	Pump Pwr [W]	PV Area [m²]	Batt. Cap. [Wh]	Tank Vol. [m³]
0.125	1	29	0.10	12.5	0
0.25	2	46	0.46	0	0
0.5	3	74	0.76	0	0
0.75	3	118	1.23	0	0
1	4	180	1.83	0	0.005
1.5	5	295	3.00	0	0
2	6	636	6.47	0	0

Moreover, in the right bar it can be seen that the initial capital cost is the majority of the total life cycle cost. In fact, the IC makes up over 50% of the total cost and over 70% for many of the cases. Therefore, if the initial capital cost of the system could be reduced through subsidies or other programs, the total LCC would be greatly reduced. In addition, the maintenance cost is always lower than the replacement cost and initial cost. The maintenance costs are based off labor costs for the location (Appendix A.2), and because the labor cost is low in these areas the maintenance cost is low [15, 16]. Both maintenance and replacement costs increase with field area, although there is only a slight increase in replacement costs from the 0.125 to the 0.25 ha case. These costs are comparable because the former has batteries whereas the latter does not, and the replacement cost of batteries is high. The replacement cost is also higher than the maintenance cost for all of the cases because a portion of the hydraulic network and the panels, which make up some of the highest component costs, are replaced over the lifetime of the system. For all of the field areas the LLP is between 0.1 and 0.15, indicating that going to the maximum LLP minimizes the life cycle cost, as expected. The changes in LLP are due to the mechanics of the algorithm, the cost benefit gained for an increase in LLP from 0.1 to 0.15 is not large enough to cause further iterations in the optimization before convergence is reached. The LLP limit is explored further later in the section and compared back to this analysis.

Analyzing how the life cycle cost of the system changes with field size gives an
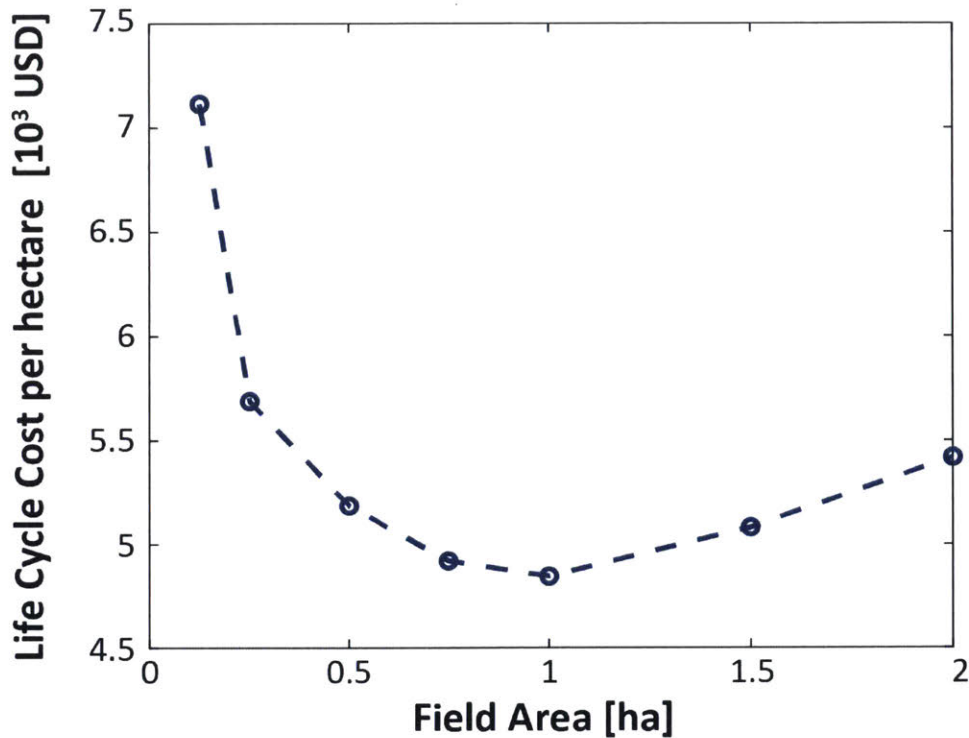
Figure 4-2: The LCC per ha of the optimal system designs. This shows economies of scale when expanding up to 1 ha, after which there are diseconomies of scale. For this case study, the 1 ha field has the optimal LCC per ha design.

initial idea of the economies and diseconomies of scale for solar powered drip irrigation systems. This is explored further in Figure 4-2, in which the cost per hectare for the optimum LCC at each field area is plotted against the field area. The cost per hectare decreases as field area increases until the 1 ha case, after which the cost per hectare increases with increasing field area. This means it is most cost effective to install a solar powered drip irrigation system on a 1 ha field for this sample case study.

In order to explore when energy storage becomes an option for the sample 1 ha case, a sensitivity analysis is conducted to see how the optimum life cycle cost and energy storage of the design changed while changing panel area. Figure 4-3 shows this analysis with the optimum LCC and LLP plotted. The panel area increases in increments of 0.1 m^2. The hydraulic component is not included in the bar chart because the field area is held constant, so the hydraulics cost is also constant. The pump component cost is constant in this study as well, due to the fact that the system operation point is constant.

The panel cost increases linearly with the panel area, as expected (Eq. 3.47). The reliability constraint ($LLP = 0.15$), tank constraint, and battery constraint, ensure there is a minimum possible panel area. In this case, the minimum panel area is 0.6 m^2. The optimum designs sometimes include tanks, but these tanks are very small, and as previously stated, this is most likely an artifact of the optimization, as tanks this small would not be realistic in an actual system. The battery cost decreases with increasing panel area. This is because as panel area increases, less additional energy storage is needed to meet the reliability constraint on the system. Eventually with a high enough panel area, no energy storage is needed to meet the constraint. After there is enough panel area to meet the system reliability constraint, an increase in panel area causes an increase in the total LCC and a decrease in LLP. This is shown in Figure 4-3 after 1.8 m^2.

The minimum LCC occurs at 1.8 m^2 with a very small battery, and is essentially a direct drive case, as a battery capacity that small is not realistic. Although the optimal design is direct drive, some of the designs with batteries have comparable LCCs to the optimum, such as the 1.2 m^2 case. Although these designs have unrealistically small energy storage options, energy storage allows for more flexibility in the time of day irrigation could occur, which could be beneficial in some regions or for some crops. Running this analysis with further restrictions on irrigation start time or schedule may produce optimal solutions with realistic energy storage options. In future analyses the trade-off between using energy storage and irrigating at different times of the day can be explored further with this model.

The cost-optimization was run for the same set of field sizes as above with emitters rated for 2, 4, 6, 8 and 10 Lph at each field size. The LLP limit was set to 0.15. The minimum LCC system was selected for each field size and plotted against the corresponding emitter flow rate (Figure 4-4). The goal is to find the optimal emitter flow rate for each field size and demonstrate the capability of the model to inform low-pressure emitter design. At the lowest flow rate, the system needs to irrigate for longer in order to meet the water demand reliably, and at the highest flow rate, the system will need to provide the most power to operate at the high flow rate.
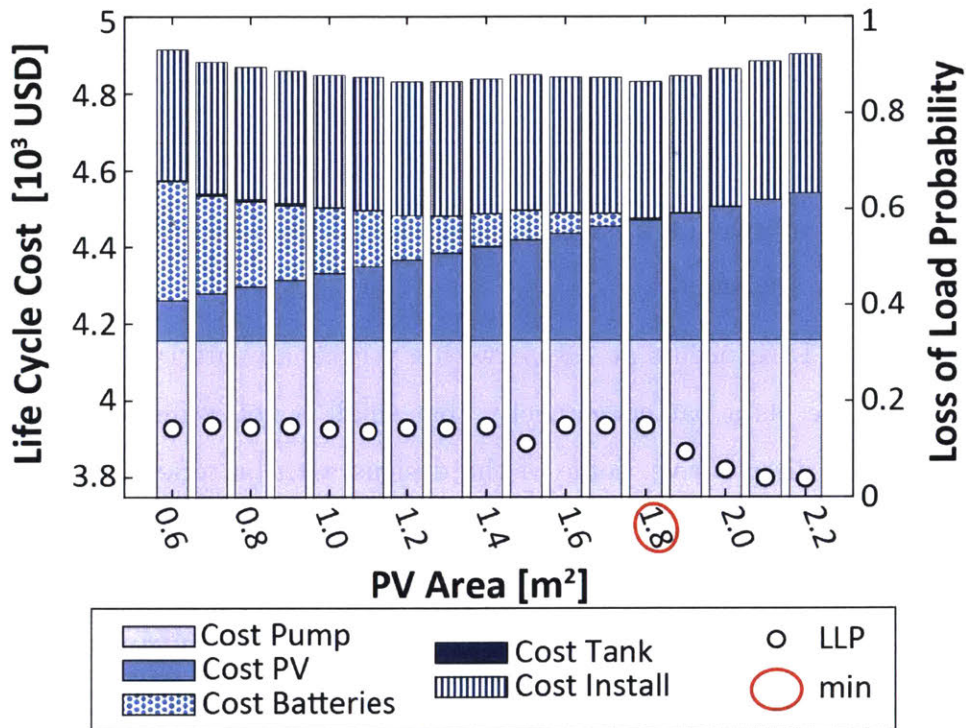
Figure 4-3: The sensitivity of the system LCC for the 1 ha sample case to panel area. Each design is an optimum for a given panel area. For small arrays, batteries and very small tanks are included in the design. The overall minimum cost system is effectively a direct drive system. After this optimum, the LLP drops considerably as more capacity is added to the power system.

The result shows that the 2 Lph emitter system is the lowest cost for the 0.125 ha field. This implies that it is cost effective to build a system with the required energy capacity to run at a low flow rate. The result also shows that the 8 and 10 Lph emitters are not optimal for any of the field sizes. This is because, at higher flow rates, the system needs to have a larger pump and a higher power capacity in order to operate a higher flow rate drip network.

The oscillation between 4 and 6 Lph emitter optimums is an indication of the limitations of using the model in its current form for selecting an optimal emitter flow rate. Because the pump selection is discontinuous by nature, the cost difference between pumps could be driving the cost difference between 2 to 6 Lph emitter systems. This makes it difficult to say whether these are definitively the optimal emitter flow rates at each field size. A more thorough method would require some cost relationship that defines the price of the pump as a function of its characteristic performance. Then cost would be directly linked to the behavior of the pump and have a more realistic impact on the optimal emitter flow rate result. With a discrete pump selection, the most that can be concluded from this analysis are the bounds of the optimal emitter flow rate search. It shows that, for this range of field sizes, the mid-range flow rates are preferable to those that require a high energy or high power capacity from the system.

The sensitivity of the cost-optimization to changing the system reliability requirement is explored by increasing the LLP limit from 0 to 0.5 for 0.125 ha, 1 ha and 2 ha fields. The average reliability over the season is the inverse of LLP, which is defined in Equation 3.55. An $LLP = 0$ corresponds to 100% of the demand being met over the course of the season and an $LLP = 1$ corresponds to none of the demand being met. As expected, Figure 4-5 shows that it is most expensive to design a system with an $LLP = 0$, or 100% reliability. If the LLP limit is relaxed slightly to 0.1, the system life cycle cost drops by 7%, 9% and 13% for the 0.125, 1 and 2 ha cases, respectively. Based on the yield curve shown in Figure 3-13, the olive trees will still have a 100% yield at 85% of their water demand. For this reason, the LLP limit for all the simulations was set to 0.15, which enables a lifecylce cost reduction without
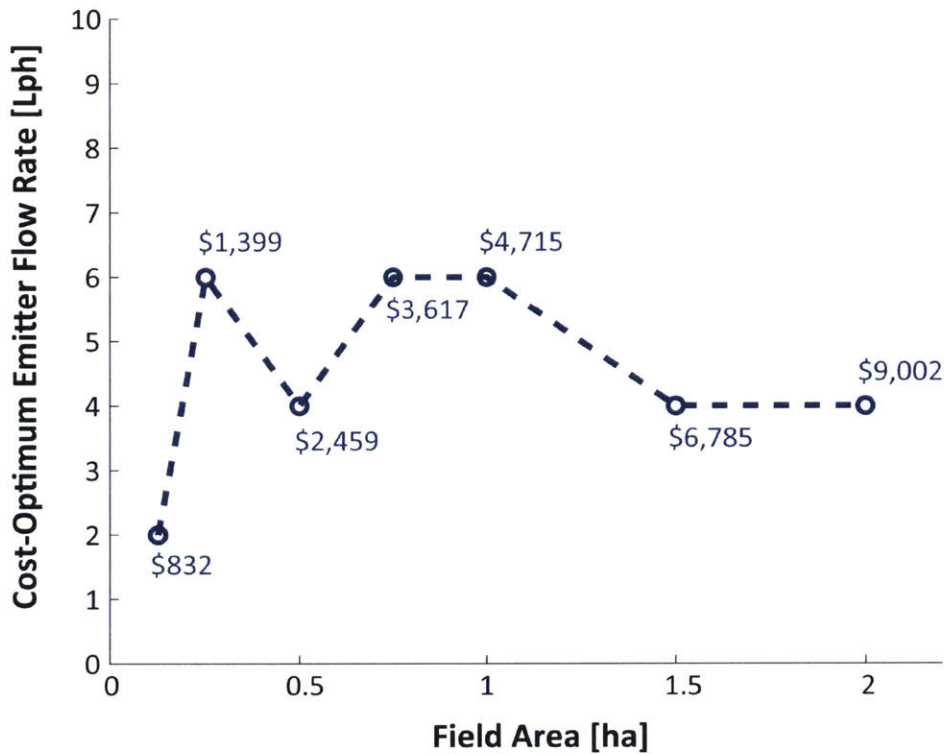
Figure 4-4: The cost-optimum emitter flow rate for each field area. The 2 Lph emitter is only cost effective for the smallest field because the larger fields would require energy storage to meet the reliability requirement at such a low flow rate. The 8 and 10 Lph emitters are never the optimum because the power system capacity required to run at such a high flow rate is expensive. The optimal emitter flow rate of the remaining cases oscillates between 4 and 6 Lph, likely because the discrete pump selection becomes the primary cost driver in the optimization. For these field sizes, the mid-range flow rates are optimal. The LCC of each optimum system design is labeled in the plot.
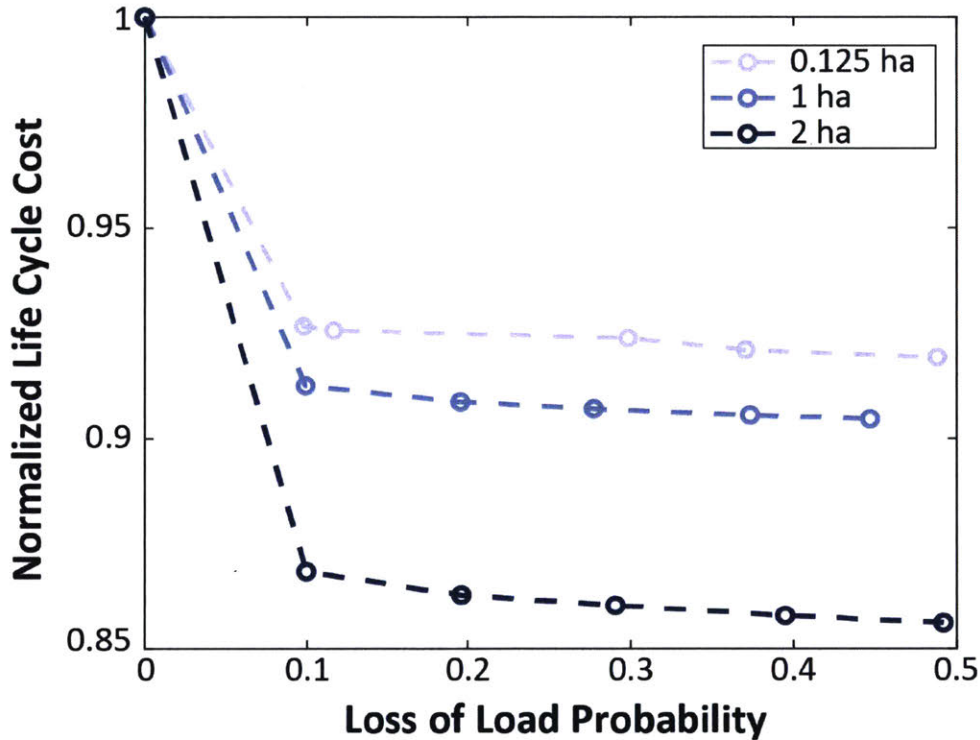
Figure 4-5: The LLP limit is varied from 0 to 0.5 for the 0.125, 1 and 2 ha fields to explore the sensitivity of the cost-optimization to the reliability requirement. An LLP limit of 0 is the most expensive, but the LCC of the optimal designs drops between 7 and 13% when the LLP limit is increased to 0.1. A small relaxation of the reliability requirement can significantly reduce the optimal system cost. An LLP limit of 0.15 was selected for the cost-optimization based on the olive crop yield curve that shows 100% yield at 85% evapotranspiration, which is a proxy for demand.

sacrificing any crop yield. It is important to note that setting the LLP limit does not fix the LLP, but sets a maximum loss of load that the system cannot exceed. This can be seen in the last case for each field size: although the LLP limit is set to 0.5, the actual LLP of the optimal systems is lower. It is assumed that above an LLP of 0.5, there will be no crop yield.

The system designs that correspond to the above points are shown in Figure 4-6. Here, the tank is converted into an equivalent energy capacity and combined with battery capacity to plot the combined energy storage capacity of the design. It should also be noted that the pump selection is the same for a given field size, which makes sense because the hydraulic operating point does not change. The panel area appears to be most sensitive to an LLP limit of zero, where the panel area is at its largest:

0.67, 4.3 and 15.3 m^2 for the 0.125, 1 and 2 ha cases, respectively. This is more than double the optimal panel area for an LLP limit of 0.15 at these field sizes. As the LLP limit increases, the panel area remains relatively constant for each field size. Three of the designs for the 0.125 ha field and one of the designs for the 1 ha field have some energy storage capacity, although in these cases, it is less than the energy storage capacity of six AA batteries. Effectively, these are all direct drive systems. At the LLP limit of 0.15, it appears that the optimal system for all field sizes is a direct drive system or a system with a very small energy storage capacity. This is confirmed by the results of the field area sensitivity analysis.

Finally, a sensitivity analysis was run to see how a change in reliability affects the system design when optimized for profit. A change in reliability lowers the amount of water delivered to the crops and therefore can lead to a reduction in yield. To account for this reduction, the objective was changed to optimize for profit, and account for the crop revenue earned over the system lifetime. Figure 4-7 shows the sensitivity of the optimal system profit for different field sizes, and is comparable to Figure 4-1. Note that for Figure 4-7 the cost and profit are normalized by the 1 ha sample case so that they can be easily plotted together. Table 4.2 shows the corresponding optimal designs. By comparing the two studies it can be seen that the system costs and optimal designs, whether optimizing for profit or LCC, are very similar.

As expected, the cases with the same field area have the same hydraulics cost, and all of the chosen pumps are the same. The panel area, and therefore cost, is slightly larger for all of the profit optimized cases compared to the LCC optimized cases. This likely because the profit-optimization is less sensitive to small changes in component capacities (Section 4.3). The 0.125 ha case is still the only case with battery capacity, although it has a smaller capacity than one rechargeable AA battery, and all other cases are direct drive designs. The LLP is lower for all of the profit optimized cases, which correlates to the higher panel cost. Because the reliability is not a constraint, the optimum does not go to an LLP of 0.15. The LLP gets close to 0.1, which has been shown to be where a large reduction in LCC occurs (Figure 4-5). Olives are also a water stress resistant crop, so a small reduction in applied water has only a small
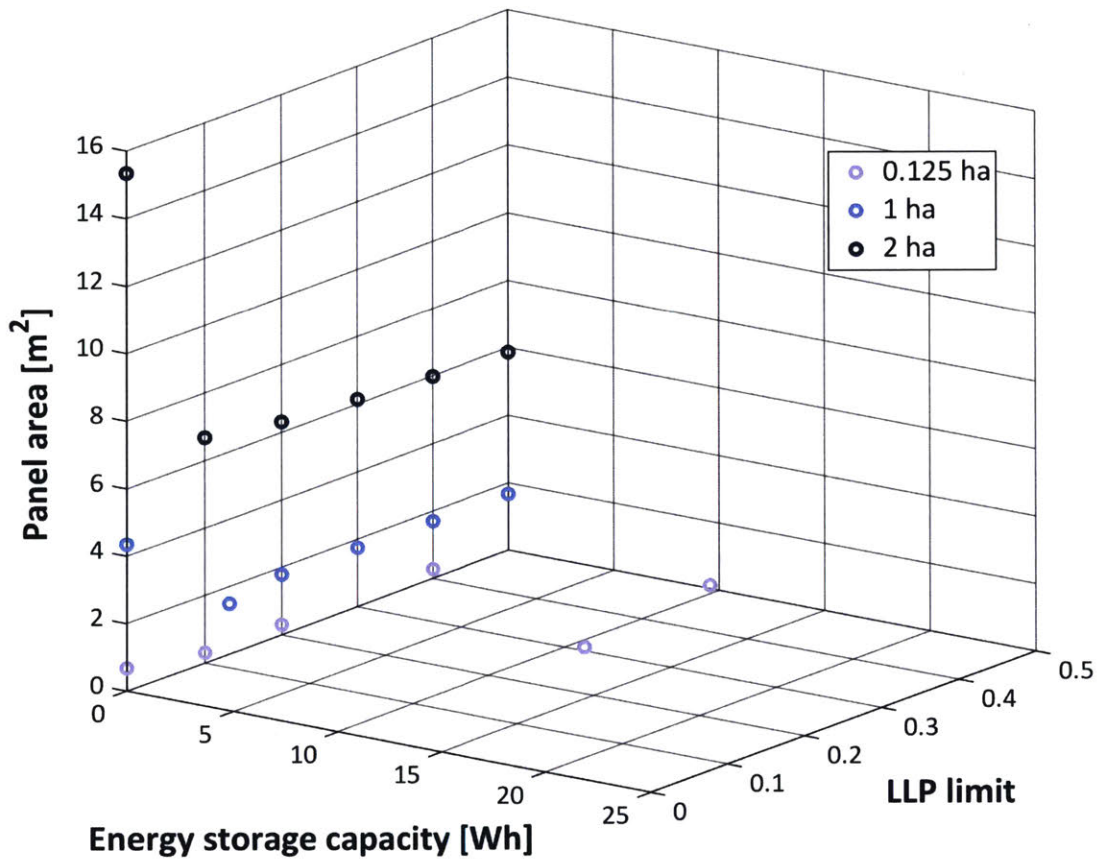
Figure 4-6: The system designs corresponding to the reliability requirement sweep show that the majority of the systems are direct drive. For an LLP limit of 0, the optimal systems have a panel area of 0.67, 4.3 and 15.3 m^2 for the 0.125, 1 and 2 ha cases, respectively. This is more than double the optimal panel area for an LLP limit of 0.15 at these field sizes. For the few designs that do have energy storage options, the capacity is less than that of six AA batteries, so all the designs are effectively direct drive.
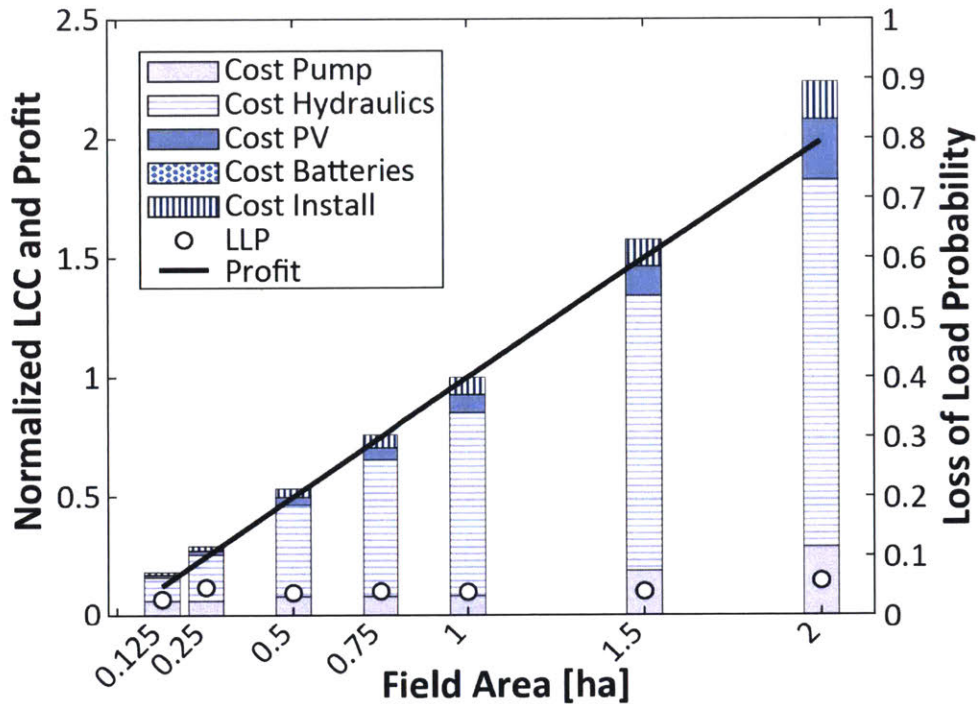
Figure 4-7: The sensitivity of the optimum profit to field size, where the profit and LCC are normalized to the 1 ha case. The profit-optimization produces direct drive designs with slightly larger panel areas than the cost-optimization. The profit is approximately an order of magnitude larger than the cost, so this optimization scheme is less sensitive to small changes in component capacity. There is no imposed LLP limit; the crop yield model, which links the water delivered directly to revenue, acts as the reliability constraint.

effect on the yield (Figure 3-13) and therefore revenue.

It should be noted that the revenue and profit are an order of magnitude larger than that LCC for all the cases. The revenue increases linearly with field area since the LLP is similar between cases, the yield is similar, and the crop price and interest and inflation are constant for the same location and crop (Eq. 3.42). The order of magnitude difference means that profit effectively increases linearly with field area, so the objective will favor maximizing revenue over minimizing cost. An additional objective could be made in future studies with a weighting factor that allows for cost to be considered more of a driving factor compared to revenue.

The insight gained from this sensitivity analysis justify the current construction of the model and offer a broader context for the design solutions. The optimal system design is direct drive in the pertinent field size range, and these systems are most cost

Table 4.2: Optimum Profit Design for Various Field Sizes

Field Size [ha]	Pump No.	Pump Pwr [W]	PV Area [m²]	Batt. Cap. [Wh]
0.125	1	29	0.31	1.5
0.25	2	46	0.52	0
0.5	3	74	0.86	0
0.75	3	118	1.37	0
1	4	180	2.10	0
1.5	5	295	3.45	0
2	6	636	7.04	0

effective for a field size of 1 ha. The initial cost of the system makes up the majority of the life cycle cost, indicating that subsidies could be an important step towards increasing adoption of this technology among smallholder farmers. The hydraulic network is the most expensive component and could be geometrically optimized to reduce the system cost further. The most cost effective emitter flow rates for this field size range are between 2 and 6 Lph, which indicates this model may be able to inform future emitter design. Finally, increasing the LLP limit slightly, and thereby relaxing the reliability requirement, leads to a significant drop in the life cycle cost of the optimal system design without significantly reducing the crop yield.

4.3 Robustness & Objective Function Sensitivity

In addition to assessing the model sensitivity, the optimization was subjected to a set of simulations designed to assess the robustness of model. The repeateability of the optimization algorithm convergence was tested, the sensitivity of the objective function to key cost equation parameters were explored, and the sensitivity of the solution to changes in weather input data was analyzed. The optimization was found to converge repeatably and within a reasonable amount of time for all the tested field sizes with a swarm size of 20 and a convergence margin of 10 USD. The objective function is most sensitive to the initial cost factor, k_i, and maintenance cost factor, k_{OM}, for the cost optimization, and most sensitive to the crop price factor, k_{cp}, for

the profit optimization and, as a preliminary estimate, the weather robustness factor is 1.33 for the 1 ha sample case.

The convergence repeatability of the PSO algorithm was first tested by running the model for the sample case for different values of two parameters: the swarm size, N, and the convergence margin, e. The swarm size is the number of potential design solutions the algorithm tests at one time, and the convergence margin is the maximum amount the objective value of two solutions can differ for convergence to be declared. Here, the value of the objective function is the cost and the convergence margin is in units of USD. Essentially, these two parameters control how the PSO starts and how it stops. The model is run for four combinations of swarm size and convergence margin: $N = 10$ and $e = 50$, $N = 10$ and $e = 10$, $N = 20$ and $e = 10$, and $N = 50$ and $e = 10$. Each parameter run is repeated 5 times for a 0.125 ha, 1 ha and 2 ha field, for a total of 60 runs.

In each case, it is expected that the algorithm converges on a single solution, which means the life cycle cost should be roughly the same for a given field size. This is shown to be the case in Figure 4-8. In general, as the swarm size increases and the convergence margin decreases, the time it takes the algorithm to converge on a solution increases, and the solutions also become more clustered together. This indicates that as the swarm is cast wider in the solution space and the converge criterion becomes more strict, the likelihood of converging on the same solution increases. These trends are similar across the field size range and the optimization runtimes are similar, with the larger field sizes requiring a bit more time. Based on these results, a swarm size of 20 and a convergence margin of 10 USD was selected in order to reduce optimization time, while still ensuring a reliable solution convergence.

The corresponding system designs for these points are shown in Figure 4-9. With the exception of a few outliers, the runs converge on approximately the same system design for the 0.125 and 1 ha cases. For the 2 ha case, there seem to be two minimum cost solutions, with the direct drive design having a tighter convergence. This is also where four of the five runs for $N = 20$ and $e = 10$ converge. It appears that a swarm size of $N = 50$ is too large and worsens the ability of the algorithm to converge on

(a)

(b)

(c)
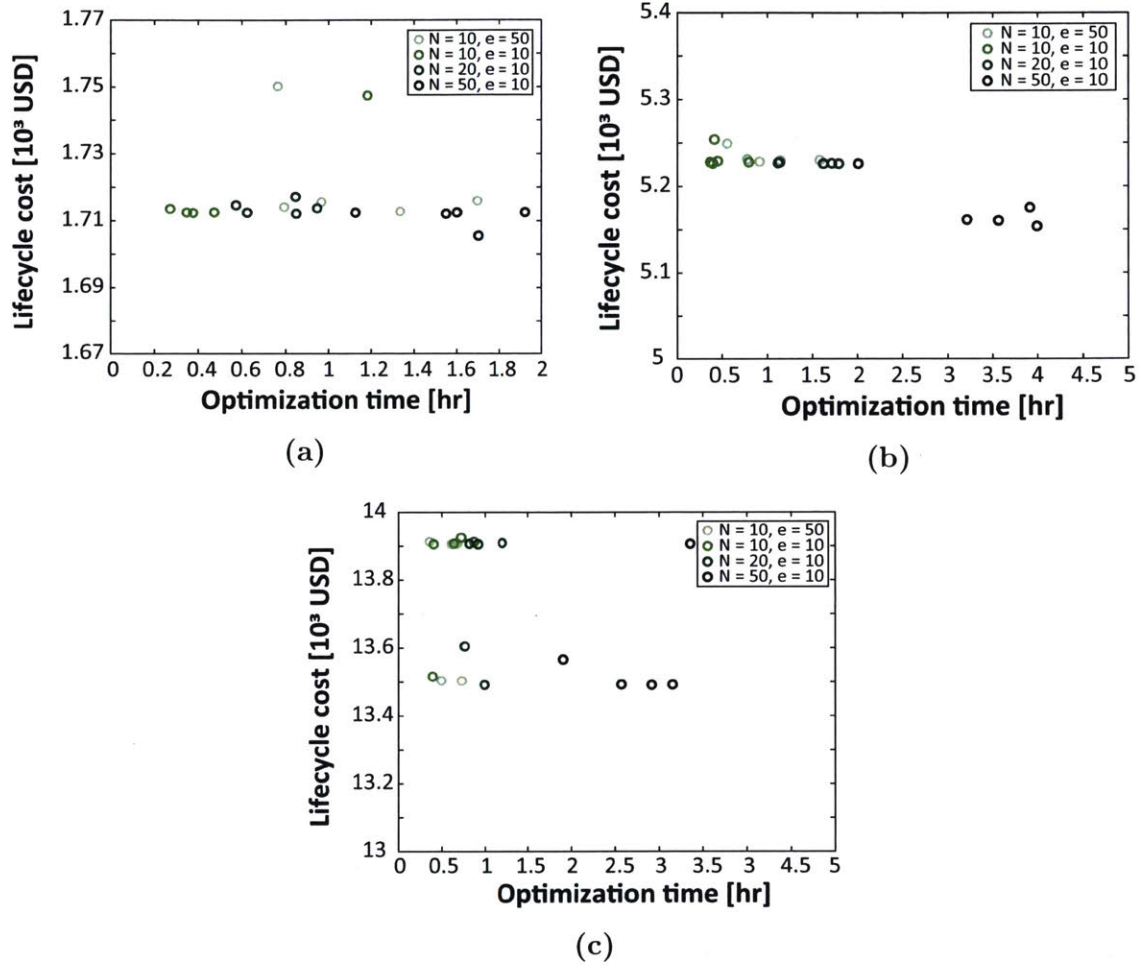
Figure 4-8: The convergence repeatability of the PSO is tested for the (a) 0.125, (b) 1 and (c) 2 ha field sizes while minimizing LCC. Four combinations of the swarm size, N, and the convergence criterion, e, were each run five times per field. The runs converge on an LCC. Typically, for a larger N and smaller e, it takes longer for the optimization to converge.

one solution for a convergence margin of $e = 10$.

In order to determine the objective function sensitivity to its data-driven cost parameters, the derivative of the objective function with respect to these variables is analyzed. The derviates are mostly linear so it is simple to determine the parameters that will have the most impact if they are inaccurate. When optimizing for cost, the objective is most sensitive to the initial cost fraction, k_i, and the maintenance cost fraction, k_{OM}. It is less sensitive by an order of magnitude to the panel and tank unit cost, UC_{PV} and UC_{tank}, and the pump, panel and tank maintenance fractions, k_{pump}, k_{PV} and k_{tank}. It is the least sensitive to the battery unit cost and maintenance fraction, UC_{batt} and k_{batt}, because the typical battery capacity is much lower than that of the pump, panel or tank. When optimizing for crop, the objective is the most sensitive to the crop cost fraction, k_{cp}, because the revenue is about an order of magnitude larger than the cost. This means that more data on the initial cost of the system and the local crop prices must be collected in order to produce an accurate cost model.

The input weather data is what ties the system design solution to the given location. The weather determines both the available power to the system as well as crop water demand. Several of the important weather parameters are shown in Table 4.3. These are averages to give a sense of scale, but all the datasets used in this study have a resolution that is hourly or higher. It is assumed that the weather for the entire season is known a priori, which vastly simplifies the task of modeling the system operation. This is of course not the case in the real world, especially as the effects of climate change are altering historical weather patterns. In all the simulations, hourly typical meteorological year (TMY) data are used. This is a dataset that takes the "most typical" weather from at least 12-25 years of data and creates an average weather year of sorts.

In order to determine the robustness of the solution to different weather inputs, the 1 ha sample case is run with the TMY data and three other sets of weather data from Morocco: historical data from 2014 and 2016, and measured data from the Moroccan field trial site in 2018 (Chapter 5). The 2014 and 2016 data were

88

(a)

(b)

(c)
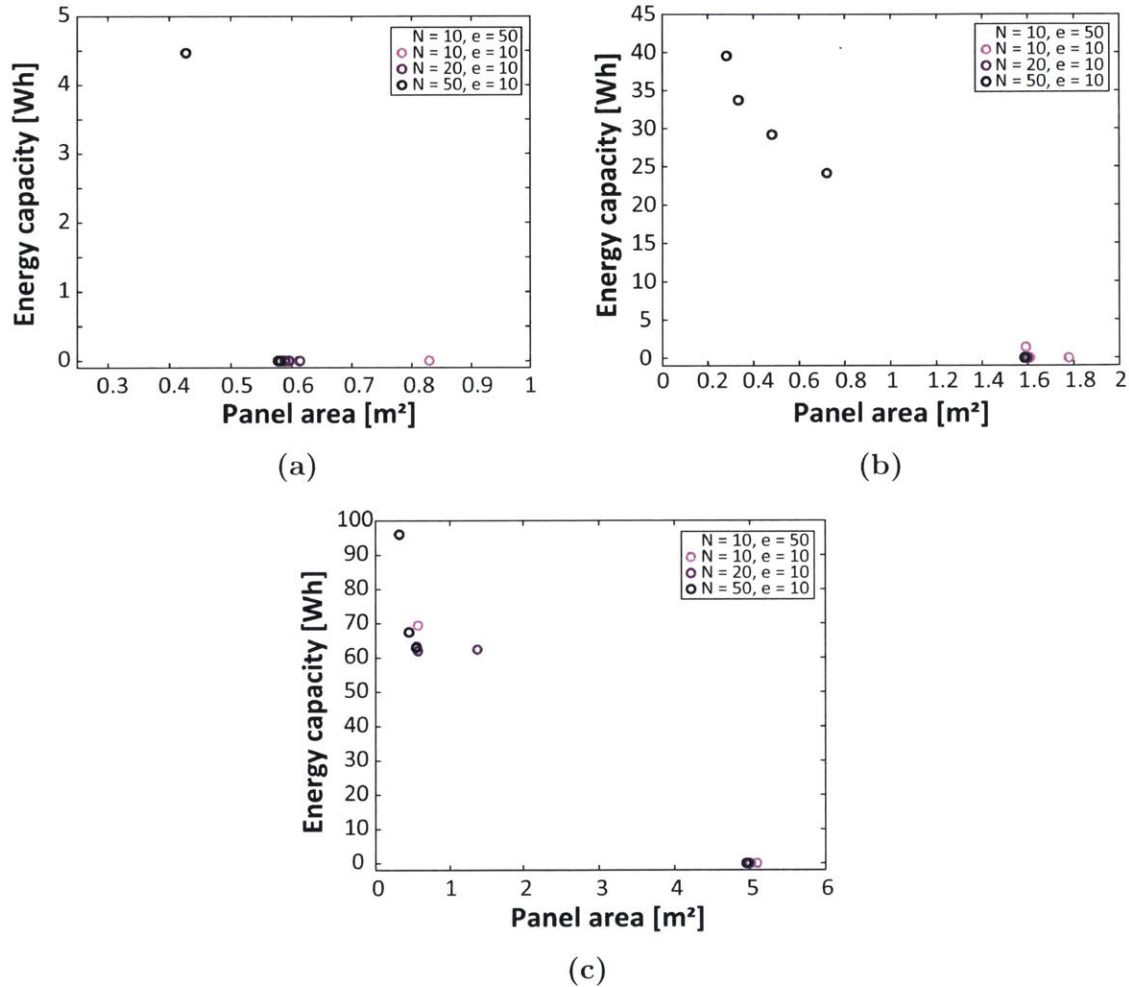
Figure 4-9: The corresponding system designs for the PSO repeat runs minimizing LCC. Aside from a few outliers, the runs converge on approximately the same system design for the (a) 0.125 and (b) 1 ha cases. For the (c) 2 ha case, there seem to be two minimum cost solutions, with the direct drive design having a tighter convergence. A swarm size of $N = 50$ appears to be too large and worsen the ability of the algorithm to converge on one solution for a convergence margin of $e = 10$. $N = 20$, $e = 10$ converged tightly and reliably in a reasonable amount of time, so these parameters were selected for the PSO.

Table 4.3: Weather Data Averages

Weather Parameter	TMY	Hist. 2014	Hist. 2016	Meas. 2018
Avg. Irradience [$\frac{W}{m^2}$]	250	264	236	227
Avg. Temp. [C]	22.5	22.0	22.1	20.8
Avg. Rel. Hum. [%]	54	55	56	62
Total Rain [mm]	137	97	101	6
Avg. Wind Speed [$\frac{m}{s}$]	2.5	1.4	1.0	3.4
Avg. ET0 [$\frac{mm}{day}$]	5.6	4.9	4.3	6.0

included because Morocco experienced a drought in both years [45, 46]. The TMY and historical weather data, sourced from [30], all have an hourly resolution, and the measured data has five-minute resolution. All of the cost-optimized designs are subject to the same reliability constraint with an LLP limit of 0.15. The resulting designs for each dataset are shown in Figure 4-10. The hydraulic network cost is removed for clarity because it is not optimized and therefore is known to remain constant for the same system. The installation cost is a fraction of the hydraulic cost and the selected pump is the same, so the cost of both also remain constant.

Interestingly, the case using the TMY data sizes the largest system, with a panel area of 1.9 m², which indicates that using this conglomerate data may produce an oversized system for some years. The historical data cases produce slightly smaller 1.6 m² direct drive systems. These were drought years, which means there was more solar power available, but the temperatures were also higher, which would increase evapotranspiration and crop water demand. The LLP of the TMY case is 0.1, whereas the 2014 and 2016 cases have LLP values of 0.14 and 0.15, respectively. It appears that increasing the LLP slightly to compensate for increased evapotranspiration is enough to balance having a smaller panel area to take advantage of the higher solar irradiance at the expense of meeting less of the water demand. The measured data produces the smallest panel area, 0.73 m² and a battery capacity of 8 Wh, which is equivalent to the capacity of about three AA batteries. Since this energy storage capacity is so small, its reasonable to say that the optimal design in all four cases is essentially a direct drive system.

Although it was somewhat surprising that the drought year weather data produced lower cost designs, this process can be used to define a design "robustness factor" to account for weather variations. Assuming these are all direct drive systems, the optimal panel capacity is 1.5 ± 0.5 m^2. The standard deviation represents a $\pm 33\%$ change in the panel area. To generalize this, a robustness factor of 1.33 should be applied to an optimal direct drive design produced using TMY one weather dataset before it is actually built. This factor becomes more useful for a larger number of test cases and datasets, but the method remains the same. Even with this additional factor, the optimized solution, at 2 m^2, has a significantly smaller panel area than the conventionally designed system, which is calculated in Section 4.1 with a panel area of 5.3 m^2. This represents a 62% reduction in the system cost compared to the conventionally designed system, if all other components are equal.

Another interesting result was that the measured weather data with five-minute resolution produced the smallest optimum design. The measured 2018 weather data had the lowest irradiance and very little precipitation. The latter may be due to a sensor malfunction, but this low precipitation measurement was used to size the system in simulation. In spite of this, the optimized system was the cheapest of all four cases. This indicates that having higher time step resolution when simulating the operation of the drip system allows the algorithm to take advantage of the component capacities more efficiently, resulting a smaller, less expensive design. The benefits of higher weather data resolution, as well as expanding simulated system operation capabilities of the model, should be explored further.
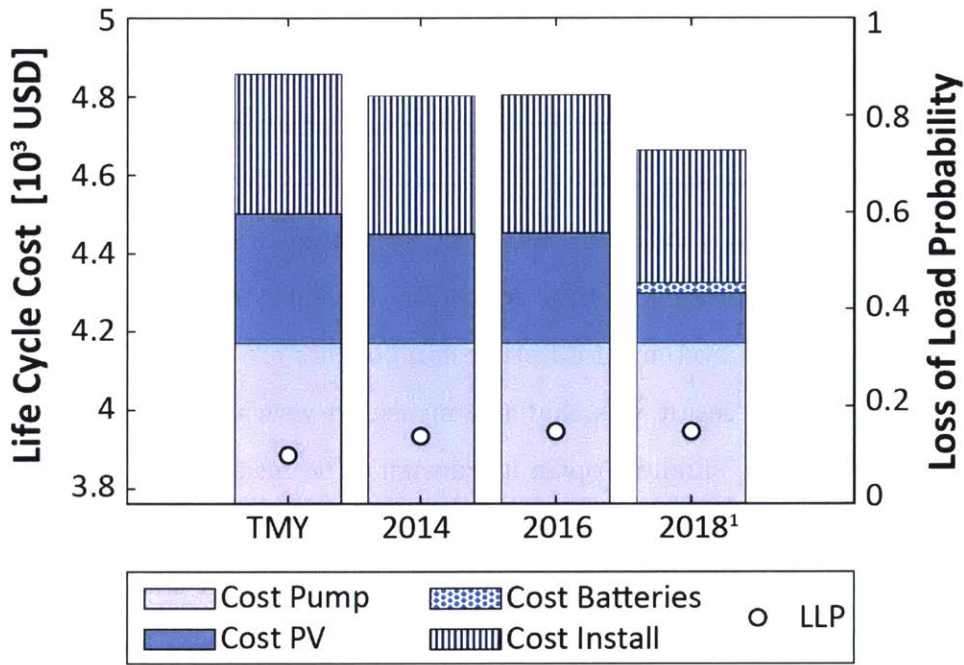
1. 2018 data was measured in our field trials and is in 5 min intervals while the rest of the weather data is hourly

Figure 4-10: The sensitivity of the cost-optimum result to varying weather conditions for the 1 ha sample case. The TMY data (hourly) produces the most expensive optimum design. The data from two drought years (hourly) produces slightly less expensive designs. The LLP is larger in these years indicating a trade-off between taking advantage of the higher irradiance by reducing panel area and meeting less of the crop water demand. The measured 2018 weather data (five-minute) produces the least expensive design, indicating possible further cost reduction using higher resolution weather data. The design variation suggests a preliminary "weather robustness factor" of 1.33 for direct drive optimum designs.

Chapter 5

Field Trial Results

5.1   Field Trial Methods

Field trials are being conducted in Morocco and Jordan to test and analyze drip irrigation systems. These field trials have been ongoing since 2017 to test the ultra low-pressure emitters [18]. In 2018, two of the systems were retrofitted with solar panels and a solar pump. One solar powered system was installed in Sharhabeel, located in the Jordan Valley, and another was installed in Saada in Marrakesh, Morocco. The purpose of this part of the field trials was to see if solar powered pumping systems could be used with the ultra low pressure emitter systems, and to validate the model presented in this thesis as a system design tool. For both locations, a commercially available solar pump was installed. The pump was oversized in order to allow for the systems to operate in unknown weather conditions and because making a custom system was not within the original scope of the project. Therefore, the results of these field trials are used to validate the model simulation, but not the optimization. In future trials the optimization model can be used to design a custom system. The design, implementation, and data collection of the solar powered drip irrigation systems associated with the field trials was completed in partnership with research organizations in Jordan (MIRRA) and in Morocco (ICARDA), with support from Jain Irrigation.

Figure 5-1 shows a diagram of the setup that was used. The set up of the two field

trial sites were similar with some key differences. In Sharhabeel, the MIT designed ultra low-pressure online emitters were tested on a 0.16 hectare field of 64 citrus tree crops. A Lorentz PS2-600 CS-F4-3 solar surface pump system was installed and connected to two Jain (JJ-M672-300Wp) solar panels. The reservoir was located 1.5 meters below the inlet of the pump. In Saada, the testing was completed on a 0.52 hectare field of 90 young olive tree crops. A Lorentz PS2-600 CS-F4-3 solar surface pump system was also installed for this field, but it was connected to two Canadian Solar (CS6P-270Wp) panels. The reservoir for Saada was located two meters above the inlet of the pump, and provided some positive inlet pressure.

Both field trial setups pulled water from a reservoir and pushed it through a sand and disk filter and through a fertigation unit, which was used on an approximately biweekly schedule. In order to monitor the system operation, a flow sensor (Dwyer WMT2-A-C-07-10) and a pressure sensor (Lorentz LPS-500) were placed after the outlet of the pump and an additional pressure sensor was placed after the fertigation unit (SSI P51-15-G-UC-I36-20MA). The difference between the two pressure sensors allows the pressure drop over the filters and fertigation unit to be analyzed. Additionally, a manual pressure sensor was placed directly after the last emitter in the field to monitor if the last emitter was at its activation pressure. If the last emitter in the line was at activation, all other emitters in the system should be above activation and operating at the rated flow rate. The pump controller was able to monitor the power to the pump and the total flow delivered, as well as keep track of times when the pump was on, if there was enough solar irradiance to run the pump, and if the reservoir was low. A weather station (HOBO U30-NRC) was placed near each solar pumping system to monitor solar irradiance (HOBO S-LIB-M003), temperature and relative humidity (HOBO S-THB-M00x), precipitation (Davis S-RGF-M002), and wind speed and direction (Davis S-WCF-M003) at five minute intervals. The pressure, flow, and pump controller data were collected and transmitted at ten minute intervals (Figure 5-1). Additionally, both sites had local staff calculate and program the system to deliver the crop water demand on a daily basis. After the water demand was met for a day, the system would turn off automatically. The pump pressure was
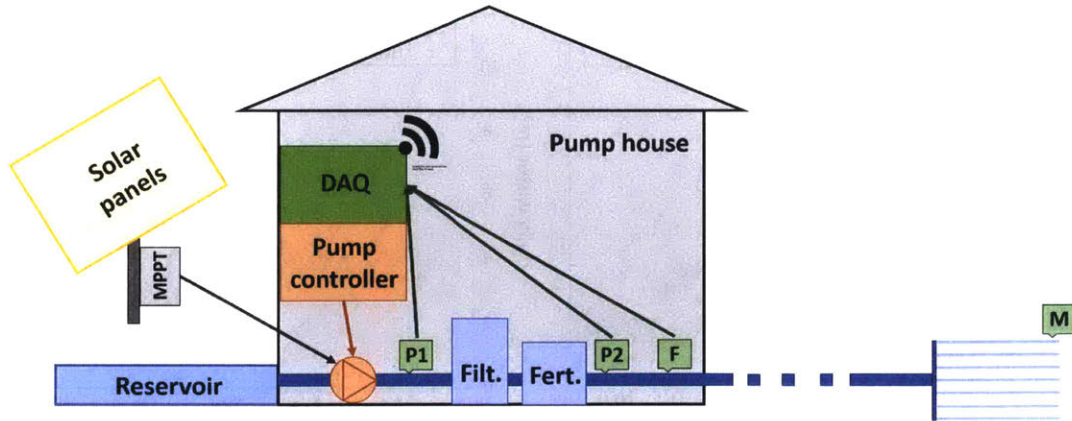
Figure 5-1: Field trial layout and instrumentation. Data recorded by two pressure sensors (P1, P2) and a flow meter (F) were transmitted every 10 minutes. A manual pressure gauge (M) was used to verify the last emitter was at activation pressure. The pump operating pressure was set based on the pump house pressure sensor reading when the last emitter was operating at its rated flow.

actively regulated by the controller. For Sharhabeel, at first the P1 pressure was set by increasing the pressure of the pump until the manometer, M, read the emitter activation pressure and the emitters were at their rated flow. Then it was noticed that the pressure drop across the filters and fertigation unit was variable, so P2 was installed to set the pressure (Figure 5-1). It was assumed that because the pressure losses after P2 were due to pipe losses and losses from the emitters, P2 would be a more stable pressure to set than P1. For Saada, the P2 pressure was set at the controller from the beginning of the trial.

5.2   Results & Model Validation

The data from the field trials in Jordan and Morocco were used to assess the validity of the simulation portion of the systems-level model. The installed systems reliably delivered water throughout the season with an LLP value of zero when compared to the simulated demand. The systems also operated within a reasonable range of the simulated system operating points in both locations. The field trials illuminated several phenomena that need to be incorporated into the model, namely the variable pressure drop across the filter and fertigation unit and the need for improved control

(a) Saada, olive trees   **(b)** Sharhabeel, citrus trees
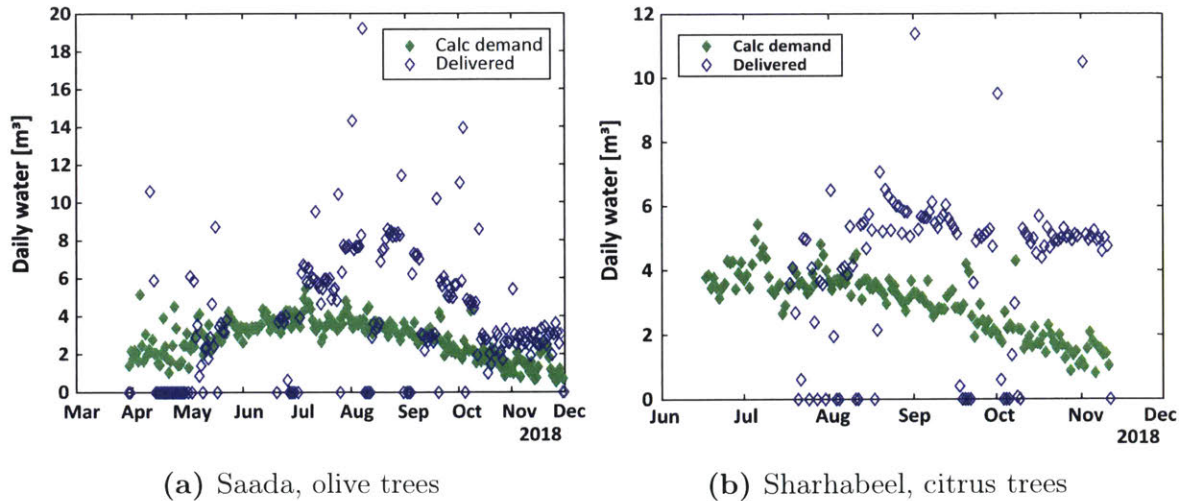
Figure 5-2: The water delivered compared to the simulated demand in Morocco (a) and Jordan (b). The season LLP calculated using the data and simulated demand was zero for both sites because the crops were overwatered.

over irrigation scheduling. Additionally, for future field trials, a pressure sensor should be added to the suction side of the pipe to better characterize the reservoir height and losses across the pump.

Figure 5-2 shows the water delivered plotted against the simulated demand during the growing season in Morocco and Jordan. The calculated LLP based on the simulated water demand was zero in both cases because the crops were slightly over watered during the irrigation season. This is partly because the local research institutions calculated water demand on a monthly basis and had control over the irrigation schedule. The research staff would decide how much to irrigate based on recent rainfall, if they had missed a day, or overwatered the previous day. The installed power systems were also oversized to ensure reliability for data collection purposes. Although the demand over the season was met, there were days with a non-zero demand where the system did not deliver water. The system was likely turned off due to recent precipitation or changes made to the irrigation schedule. Overall, the model designed two systems that performed reliably for two different crops and locations.

The field data were also used to determine the validity of the hydraulic network simulation. The pressure and flow rate were measured over the season and compared to the simulated operating point (Figure 5-3). Ideally, these points should collapse

96

onto the simulated operating point, but both the flow rate and pressure have un-avoidable fluctuations. The PC emitters operate at $\pm 7\%$ of their rated flow rate, which means the system flow rate is expected to vary by this amount. The iterative flow calculation used in the hydraulic simulation estimates the flow rate in a pipe network within $\pm 15\%$ of the actual value, which adds an additional error band to the predicted flow rate [32]. The pump operating head will be lowest when the filters are clean and the fertigation unit is not in use, and highest when operating with dirty filters during a fertigation event. The ideal operating point, along with these error bands, are shown in Figure 5-3. Each point is qualified with error bars showing the sensor measurement errors. In both cases, the majority of the data are within the expected operating range for flow and pressure. In Saada, the pump tends to operate at a lower pressure than simulated and in Sharhabeel the pump tends to operate at higher pressure than simulated, but overall the simulation appears to be accurately predicting the operating behavior of the hydraulic network.

There are several possible explanations for the data that are outside the expected ranges. There are some data points that have a higher pressure and higher flow than expected and some that have a higher pressure and lower flow rate than expected. In both cases, the higher pressure is mostly likely due to the research staff setting the pump operating pressure slightly too high. In the cases where the flow rate is also higher than expected, this is either due to erroneous flow meter readings, or a leak somewhere in the system, which was occasionally an issue in Sharhabeel. The flow rate being lower than expected indicates that either the pressure was not high enough for the entire network of emitters to reach activation or part of the system was closed off during testing. In order to explore this further, the pressure and flow sensor data were examined independently.

The operating pressure of the pump needed to be set such that the last emitter was at its activation pressure. As described in Section 5.1, the pump head was increased until the last emitter was operating at the rated flow. Figure 5-4 shows the simulated pump operating point, the expected range, and the measurements at P1. In Saada, the pump was frequently operating below the simulated value, but

97

(a) Saada, olive trees   **(b)** Sharhabeel, citrus trees
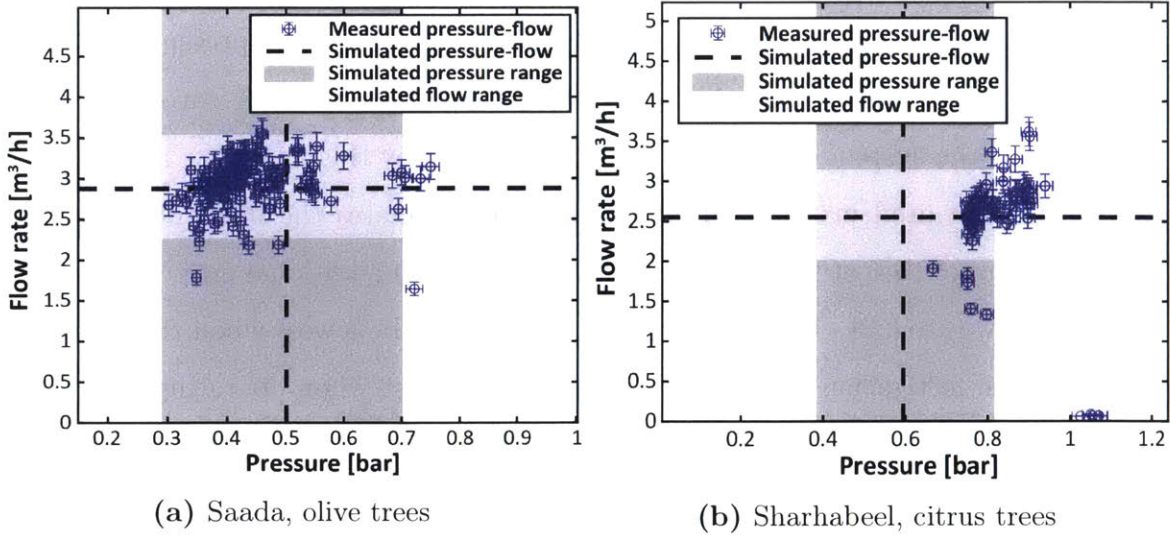
Figure 5-3: The pressure and flow rate measured over the season. The dashed line intersection shows the simulated operating point, and the grey bands show the expected variation range for pressure and flow. The PC emitters operate at ±7% of their rated flow, and the hydraulic flow calculation estimates the pipe flow within ±15% of its actual value. The pressure varies as the filters get dirty and the fertigation unit is used.

within the expected range, and in Sharhabeel, the pump was operating close to or above the upper end of the expected pressure range. In both cases, the system should deliver water uniformly, but the system in Sharhabeel appears to be over-pressurized, meaning it is operating at a higher power than necessary. This indicates that, in future trials, the pressure setpoint should be better controlled to ensure the system is operating more closely to its ideal operating point for PC behavior.

The pressure error bands were estimated based on the assumed pressure drop across the filters and fertigation unit and verified by checking the difference between the measurements P1 and P2 (Figure 5-5). The maximum pressure difference was 0.40 bar in Saada and 0.25 bar in Sharhabeel. In Saada, the gradual increase in pressure drop from around 0.05 to 0.15 bar is likely the sand and disk filter becoming dirty over the course of the season. Due to the late installation of the P2 sensor and some equipment malfunctions in Sharhabeel, there are not enough data points to notice the filter trends, but both graphs show distinct spikes, which are likely fertigation events.

The majority of the measured flow data are within the hydraulic simulation and

(a) Saada, olive trees   **(b)** Sharhabeel, citrus trees
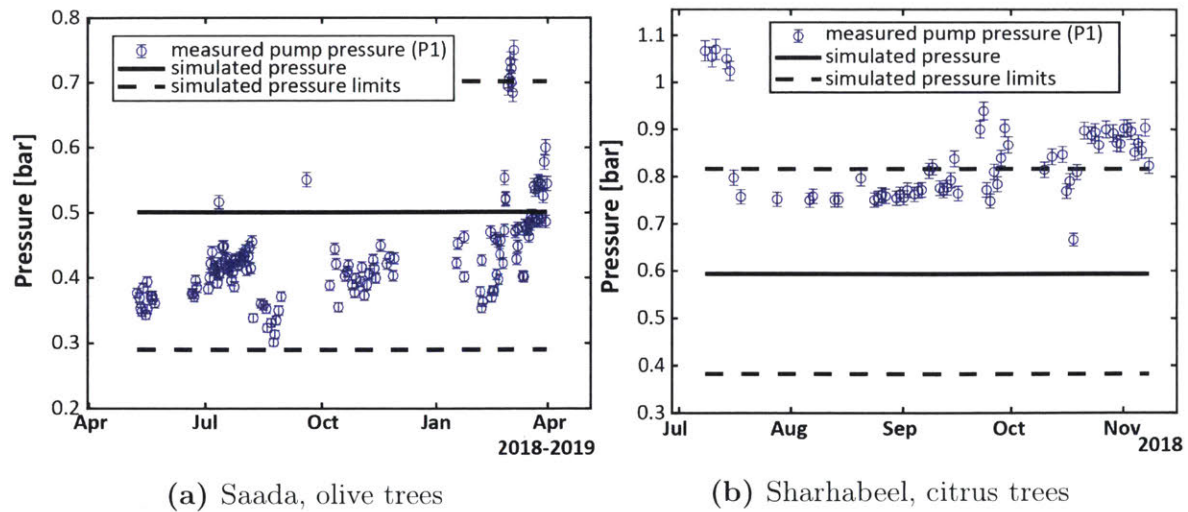
Figure 5-4: The measured pressure, simulated operating pressure, and expected range. In Saada (a), the pump frequently operates below the simulated value, but within the expected range. In Sharhabeel (b), the pump operates close to or above the upper end of the expected pressure range. In both cases, the system should have delivered water uniformly.

(a) Saada, olive trees   **(b)** Sharhabeel, citrus trees
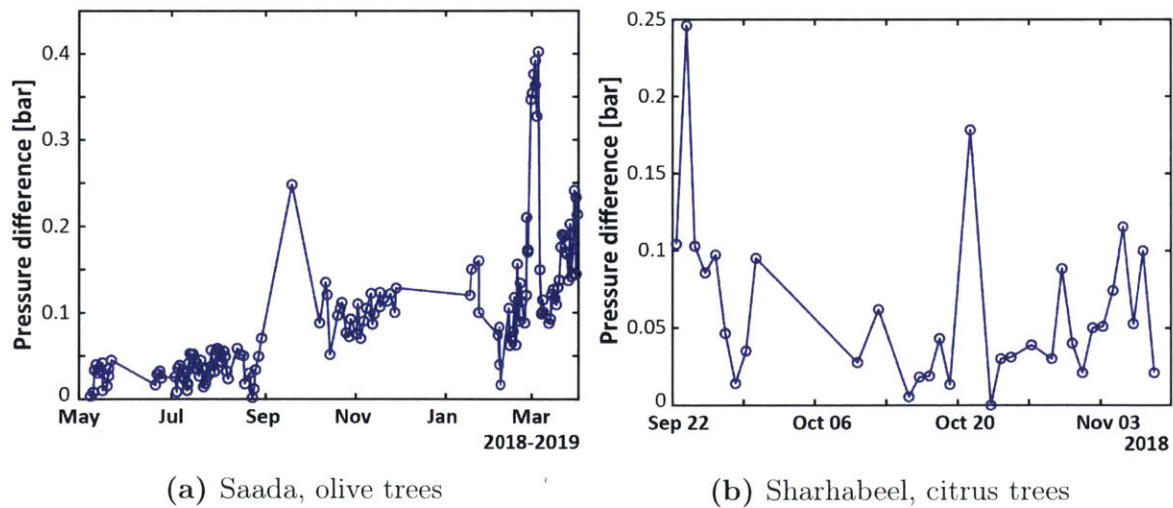
Figure 5-5: The pressure drop across the filters and fertigation unit were monitored during the season. The maximum pressure difference is 0.40 bar in Saada (a) and there is a gradual increase in pressure drop from around 0.05 to 0.15 bar, which is likely the sand and disk filter becoming dirty over the season. The maximum pressure difference is 0.25 bar in Sharhabeel (b). Both plots show distinct spikes, which are likely fertigation events.

(a) Saada, olive trees **(b)** Sharhabeel, citrus trees

Figure 5-6: The measured flow rate, simulated operating flow rate, and expected range. The points outside of the expected range correspond to lower pressures. Although these pressures are within the expected range, they still could be too low for all the emitters to reach activation. In Sharhabeel (b), the lowest flow rate points correspond to the highest pressure points, indicating some part of the system was partially closed off during testing or start-up.

emitter rated flow error bands (Figure 5-6). The low flow rate points outside of the expected range correspond to lower pressures (Figure 5-4). Although these pressures were within the expected range, they still could have been too low for all th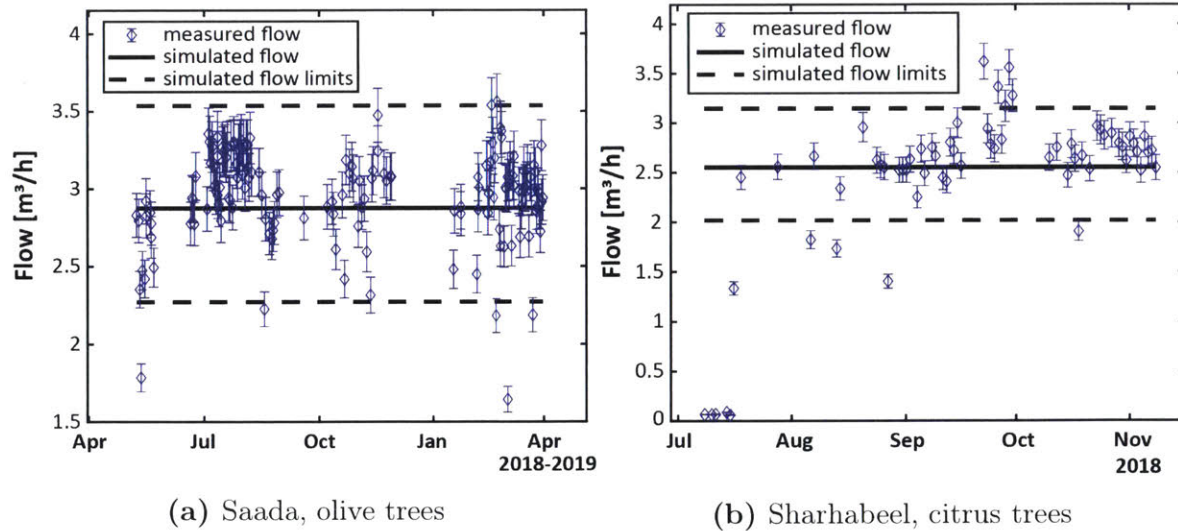e emitters to reach activation, lowering the system flow rate. In Sharhabeel, the lowest flow rate points correspond to the highest pressure points in Figure 5-4b, which indicates some part of the system was partially closed off, likely during testing or start-up.

Figure 5-7 shows the measured and simulated electrical power used by the pump for each irrigation event at Saada and at Sharhabeel. In both places it can be seen that the the measured power is higher than the simulated power limits for many of the irrigation events. The simulated power limits were calculated based on how the pressure and flow were assumed to vary, as variations in pressure and flow cause fluctuations in power. The higher power requirement of the measured data is most likely caused by the oversized system. The pump was not operating within its preferred operating range because it was oversized. Therefore, the efficiency of the pump was assumed to be higher in the simulation than it actually was in the field trials. By

100
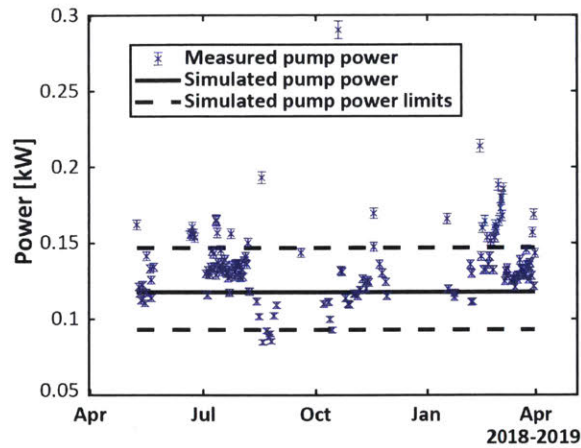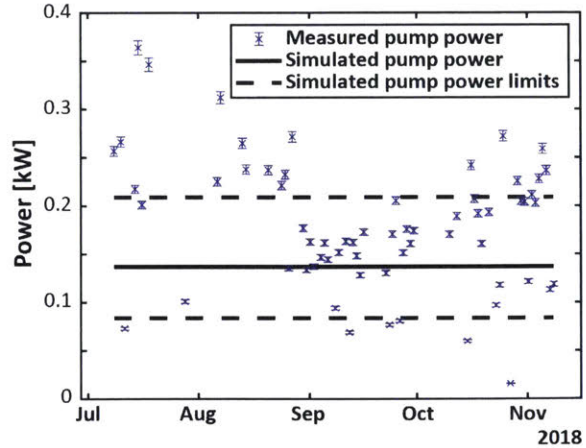
(a) Saada, olive trees   **(b)** Sharhabeel, citrus trees

Figure 5-7: The measured electrical power to the pump, simulated operating power, and expected range. For both sites, the measured power is frequently higher than the expected range. There is a higher power requirement than expected because both systems are oversized. The pump is not operating within its POR, and therefore it is operating at a lower efficiency than simulated. The average simulated pump efficiency is 36% for Saada and 40% for Sharhabeel, but the average measured pump efficiency is 27% for both sites

further analyzing the data, this was in fact found to be the case, as the average simulated pump efficiency was 36% for Saada and 40% for Sharhabeel and the average measured efficiency of the pump was 27% for both Saada and Sharhabeel.

As previously discussed, the system being oversized led to some problems, but it also ensured that the irrigation demand was met for unknown weather conditions. Figure 5-8 shows and example of good weather conditions, or a "good solar day," in which there was more than enough power output from the panels to turn the pump on and meet the demand. The system is not limited by the available solar power, but the system is oversized for this day. It also shows a "bad solar day" in which the demand was still met, but the panel power output was irregular, and so the pump would have to turn off and back on again throughout the day to meet the demand. In this case the system is limited by the available solar power and energy storage options could be utilized to meet the demand on these days if they are cost effective. Overall, these results show that the simulation is capturing the hydraulic behavior of the drip network and the energy flow through the system. In the future, having

101
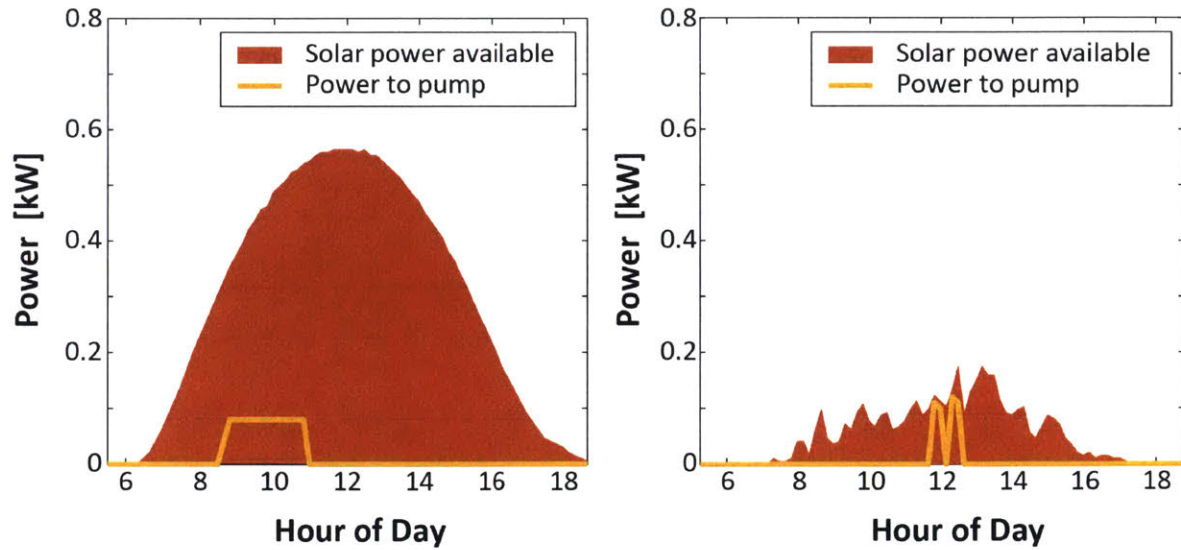
Figure 5-8: Example of a "good" and "bad" solar day. The orange shaded region shows the available power output of the solar panels and the yellow line shows the electrical power consumed by the pump. On a good solar day, the system operation is not limited by the available solar power. On a bad solar day, the system operation is limited. A system may appear to be oversized for the former, but it is sized such that it can reliably operate during the latter.

greater control over the irrigation schedule and pump operating pressure will improve the clarity of the data.

Chapter 6

Conclusions and Future Work

A systems-level model of solar powered drip irrigation systems was shown to produce optimal low cost system designs for smallholder farms. The sensitivity analysis conducted with this optimization tool indicates that optimal designs are essentially direct drive for the relevant field size range. The designs can be optimized for life cycle cost, with the LLP limit as an imposed reliability requirement. Relaxing the reliability requirement slightly for the cost-optimization significantly reduces the LCC of the optimal system design across the field size range. The system can also be optimized for profit, where the crop yield model acts as a constraint on reliability. This tool has the potential to suggest the optimal emitter flow rate for a given field size and provide a robustness factor for the design capacities to account for weather variations. The initial cost makes up the majority of the LCC, indicating that subsidies for smallholder farmers could encourage adoption of the technology. The preliminary field trials in Jordan and Morocco validate the ability of the simulation portion of the model to realistically predict the behavior of these systems.

An important next step in improving the model is collecting more local economic data to ensure the cost of the system components, crops and other parameters are accurately represented in the objective function. In future iterations of the model, more of the modules will be optimized. The hydraulic network will be cost optimized by reducing the amount of material required in the layout for the lowest possible operating point. The simulated system operation will be more flexible such that the

algorithm can decide the operation sequence based on the weather patterns and crop demand. The model also has the potential to inform pump design parameters. The pump operation throughout a representative season could be linked to its lifetime and therefore cost, ideally with a smooth function. The model could either select a pump or output the operating characteristics of an ideal pump, possibly suggesting a new pump design. The simulated hydraulic behavior can also be updated to reflect the oscillating pressure drop across the filters and fertigation unit that was observed in the field trials. In order to test these improvements in the field, a controller is being developed that can be programmed with an optimal operation scheme, but user input must first be collected to inform the key features and user interface of this controller.

In the upcoming field trials, this systems-level model will be used to design a cost-optimized drip irrigation system for each location and crop type. The robustness factor will be applied to the design capacity to account for weather variations. The custom controller will be used to mandate the irrigation schedule and regulate the pump operating pressure. The experimental performance of these systems over the course of a growing season will be used to validate the optimization component of the model, and to provide a platform for exploring the optimization of the hydraulic network and system operation scheme in the future.

Appendix A

Tables

Table A.1: Sample Case Definition

Input Parameter	Unit	Amount
Location	-	Marrakesh, Morocco
Sand/ Clay	%	25/ 35
Crop	-	Olive
Irrigation Type	-	Drip
Submain Number	-	3
Main Length	m	300
Main Diameter	mm	83
Submain Length(s)	m	75/ 75/ 50
Submain Diameter	mm	59
Lateral Length(s)	m	50/ 50/ 50
Lateral Diameter	mm	16
Crop Spacing	$m \times m$	5×5
Number Emitter	$\frac{\#}{crop}$	2
Emitter Exponent	-	0.001
Activation Pressure	bar	0.15
Added Pressure	m	4.6
Irrigation Start	-	3/1/2019
System Lifetime	$years$	20

Table A.2: Local Economic Parameters

Parameter	Morocco	Jordan
$k_{cp,Olive}$	0.55	2.12
k_i	0.11	0.45
i	0.035	0.06
inf	0.02	0.025
k_m	0.01	0.01
UC_{pump} $[\frac{USD}{kW}]$	450	450
UC_{hyd} $[\frac{USD}{ha}]$	2700	3500
UC_{emit} $[USD]$	0.2	0.2
UC_{pv} $[\frac{USD}{m^2}]$	113	103
UC_{batt} $[\frac{USD}{kWh}]$	355.32	355.32
UC_{tank} $[\frac{USD}{m^3}]$	110	110

Bibliography

[1] IFAD, "Smallholders, food security and the environment," *International Fund for Agricultural Development (IFAD)*, 2013.

[2] O. Dubois, "The state of the world's land and water resources for food and agriculture: Managing systems at risk.," *Earthscan*, 2011.

[3] J. Burney, L. Woltering, M. Burke, R. Naylor, and D. Pasternak, "Solar-powered drip irrigation enhances food security in the Sudano-Sahel," *Proceedings of the National Academy of Sciences*, vol. 107, no. 5, pp. 1848–1853, 2010.

[4] R. Sivanappan, "Prospects of micro-irrigation in India," *Irrigation and Drainage Systems*, vol. 8, no. 1, pp. 49–58, 1994.

[5] I. Mazher, S. Fayyaz-ul Hassan, H. Tamoor, N. Aadal, M. Azeem, and T. Muhammad, "Evaluation of comparative water use efficiency of furrow and drip irrigation systems for off-season vegetables under plastic tunnel," *International Journal of Agriculture and Crop Sciences (IJACS)*, vol. 7, no. 4, pp. 185–190, 2014.

[6] K. Nkya, A. Mbowe, and J. Makoi, "Low-cost irrigation technology, in the context of sustainable land management and adaptation to climate change in the Kilimanjaro Region," *Journal of Environment and Earth Science*, vol. 5, no. 7, pp. 45–56, 2015.

[7] R. Namara, B. Upadhyay, and R. K. Nagar, *Adoption and impacts of microirrigation technologies: Empirical results from selected localities of Maharashtra and Gujarat States of India*, vol. 93. IWMI, 2005.

[8] J. Doorenbos and A. H. Kassam, "Yield response to water," *FAO Irrigation and Drainage Paper No. 33*, 1979.

[9] G. Rapsomanikis, "The economic lives of smallholder farmers: An analysis based on household data from nine countries," *Food and Agriculture Organization of the United Nations (FAO)*, 2015.

[10] P. Steduto, T. C. Hsiao, E. Fereres, and D. Raes, "Crop yield response to water," *FAO Irrigation and Drainage Paper No. 66*, 2012.

[11] "Flood irrigation (image)," 2013. TNAU AGRITECH Portal Agriculture.

[12] J. Vanuga, "Irrigation methods: Furrow or flood irrigation (image)," October 2011. USDA Natural Resources Conservation Service.

[13] "Sprinkler irrigation (image)," 2009. Jain Irrigation Systems, Ltd.

[14] ICID, "Agricultural water management for sustainable rural development: Annual report 2017-2018," *International Commission on Irrigation and Drainage (ICID)*, 2017. New Delhi, India.

[15] ICARDA, "Ultra-Low Energy Drip Irrigation for MENA Countries: Drip Irrigation in Morocco," *International Center for Agricultural Research in the Dry Areas (ICARDA)*, 2017. internal report, unpublished.

[16] MIRRA, "Economics of the Agricultural Sector in Jordan," *Methods for Irrigation and Agriculture (MIRRA)*, 2017. internal report, unpublished.

[17] P. Shamshery and A. G. Winter, "Shape and form optimization of on-line pressure-compensating drip emitters to achieve lower activation pressure," *Journal of Mechanical Design*, vol. 140, no. 3, p. 035001, 2018.

[18] J. Sokol, S. Amrose, V. Nangia, S. Talozi, E. Brownell, G. Montanaro, K. Abu Naser, K. Bany Mustafa, A. Bahri, and B. Bouazzama, "Energy reduction and uniformity of low-pressure online drip irrigation emitters in field tests," *Water*, vol. 11, no. 6, p. 1195, 2019.

[19] Y. Bakelli, A. Hadj Arab, and B. Azoui, "Optimal sizing of photovoltaic pumping system with water tank storage using LPSP concept," *Solar Energy*, vol. 85, 2011.

[20] D. H. Muhsen, T. Khatib, and T. E. Abdulabbas, "Sizing of a standalone photovoltaic water pumping system using hybrid multi-criteria decision making methods," *Solar Energy*, vol. 159, pp. 1003–1015, 2018.

[21] L. C. Kelley, E. Gilbertson, A. Sheikh, S. D. Eppinger, and S. Dubowsky, "On the feasibility of solar-powered irrigation," *Renewable and Sustainable Energy Reviews*, vol. 14, no. 9, pp. 2669–2682, 2010.

[22] O. Deveci, M. Onkol, H. O. Unver, and Z. Ozturk, "Design and development of a low-cost solar powered drip irrigation system using systems modeling language," *Journal of Cleaner Production*, vol. 102, pp. 529–544, 2015.

[23] R. López-Luque, J. Reca, and J. Martínez, "Optimal design of a standalone direct pumping photovoltaic system for deficit irrigation of olive orchards," *Applied Energy*, vol. 149, pp. 13–23, 2015.

[24] R. H. Almeida, J. R. Ledesma, I. B. Carrêlo, L. Narvarte, G. Ferrara, and L. Antipodi, "A new pump selection method for large-power pv irrigation systems at a variable frequency," *Energy Conversion and Management*, vol. 174, pp. 874–885, 2018.

[25] M. G. Villalva, J. R. Gazoli, and E. R. Filho, "Comprehensive approach to modeling and simulation of photovoltaic arrays," *IEEE Transactions on Power Electronics*, vol. 24, no. 5, pp. 1198–1208, 2009.

[26] C. S. Lai and M. D. McCulloch, "Levelized cost of electricity for solar photovoltaic and electrical energy storage," *Applied Energy*, vol. 190, pp. 191–203, 2017.

[27] D. W. Bian, S. M. Watson, N. C. Wright, S. R. Shah, T. Buonassisi, D. Ramanujan, and I. M. Peters, "Optimization and design of a low-cost, village-scale, photovoltaic-powered, electrodialysis reversal desalination system for rural India," *Desalination*, vol. 452, pp. 265–278, 2019.

111

[28] W. He, S. Amrose, N. C. Wright, T. Buonassisi, I. M. Peters, and A. G. Winter, "Field demonstration of a cost-optimized solar powered electrodialysis reversal desalination system," in review.

[29] R. G. Allen, L. S. Pereira, D. Raes, and M. Smith, "Crop evapotranspiration: Guidlines for computing crop water requirements," *FAO Irrigation and Drainage Paper No. 56*, 1998.

[30] White Box Technologies, "Weather Data for Energy Calculations." http://weather.whiteboxtechnologies.com, 2008.

[31] J. Sokol, F. Grant, C. Sheline, and A. Winter, "Development of a System Model for Low-Cost, Solar-Powered Drip Irrigation Systems in the MENA Region," in *ASME 2018 International Design Engineering Technical Conferences and Computers and Information in Engineering Conference*, American Society of Mechanical Engineers, 2018.

[32] F. M. White, *Fluid Mechanics*, ch. 6. McGraw Hill, 2011.

[33] C. E. Brennen, *Hydrodynamics of Pumps*, ch. 1. Cambridge University Press, 2011.

[34] M. K. Khan, *Fluid Mechanics and Machinery*, ch. 9, pp. 513–515. Oxford University Press, 2015.

[35] D. Bian, "Optimization and Design of a Low-Cost, Village-Scale, Photovoltaic-Powered, Electrodialysis Reversal Desalination System for Rural India," Master's, Massachusetts Institute of Technology, Mechanical Engineering, August 2016.

[36] Natural Resources Conservation Service, "Soil Texture Calculator NRCS Soils." https://www.nrcs.usda.gov/wps/portal/nrcs/main/soils/survey/tools/.

[37] G. O. Schwab, R. K. Frevert, T. W. Edminster, and K. K. Barnes, *Soil and Water Conservation Engineering*. John Wiley and Sons, 1981.

112

[38] R. Hassan, B. Cohanim, and O. de Weck, "A comparison of particle swarm optimization and the genetic algorithm," in *46th AIAA/ASME/ASCE/AHS/ASC Structures, Structural Dynamics and Materials Conference*, p. 1897, 2005.

[39] C. Olcan, "Multi-objective analytical model for optimal sizing of stand-alone photovoltaic water pumping systems," *Energy Conversion and Management*, vol. 100, pp. 358–369, 2015.

[40] P. E. Campana, H. Li, J. Zhang, R. Zhang, J. Liu, and J. Yan, "Economic optimization of photovoltaic water pumping systems for irrigation," *Energy Conversion and Management*, vol. 95, pp. 32–41, 2015.

[41] P. E. Campana, A. Olsson, H. Li, and J. Yan, "An economic analysis of photovoltaic water pumping irrigation systems," *International Journal of Green Energy*, vol. 13, no. 8, pp. 831–839, 2016.

[42] M. Mohammadi, "New computing method for techno-economic analysis of the photovoltaic water pumping system using fuzzy based NSGAII optimization approach," *automatika*, vol. 56, no. 2, pp. 132–139, 2015.

[43] M. Niajalili, P. Mayeli, M. Naghashzadegan, and A. H. Poshtiri, "Techno-economic feasibility of off-grid solar irrigation for a rice paddy in Guilan province in Iran: A case study," *Solar Energy*, vol. 150, pp. 546–557, 2017.

[44] Food and Agriculture Organization of the United Nations (FAO), "FAOSTAT." http://www.fao.org/faostat/en/data/PP, 2017.

[45] S. Al-Khalidi, "Middle east drought a threat to global food prices," March 2014. Online.

[46] H. Demaree-Saddler, "Morocco grain production down 70% on severe drought," October 2016. Online.